J. Fluid Mech. (2014), *vol.* 749, *pp.* 666–700.
doi:10.1017/jfm.2014.239

Water droplet condensation and evaporation in turbulent channel flow

E. Russo[1,†], J. G. M. Kuerten[1,2], C. W. M. van der Geld[1] and B. J. Geurts[2,3]

[1]Department of Mechanical Engineering, Eindhoven University of Technology, PO Box 513, 5600 MB Eindhoven, The Netherlands

[2]Multiscale Modeling and Simulation, Faculty EEMCS, University of Twente, PO Box 217, 7500 AE Enschede, The Netherlands

[3]Anisotropic Turbulence, Department of Applied Physics, Eindhoven University of Technology, PO Box 513, 5600 MB Eindhoven, The Netherlands

(Received 14 May 2013; revised 12 March 2014; accepted 24 April 2014; first published online 22 May 2014)

We propose a point-particle model for two-way coupling of water droplets dispersed in the turbulent flow of a carrier gas consisting of air and water vapour. We adopt an Euler–Lagrangian formulation based on conservation laws for the mass, momentum and energy of the continuous phase and on empirical correlations describing momentum, heat and mass transfer between the droplet phase and the carrier gas phase. An incompressible flow formulation is applied for direct numerical simulation of differentially heated turbulent channel flow. The two-way coupling is investigated in terms of its effects on mass and heat transfer characteristics and the resulting droplet size distribution. Compared to simulations without droplets or those with solid particles with the same size and specific heat as the water droplets, a significant increase in Nusselt number is found, arising from the additional phase changes. The Nusselt number increases with increasing ambient temperature and is almost independent of the heat flux applied to the walls of the channel. The time-averaged droplet size distribution displays a characteristic dependence on position expressing the combined effect of turbophoresis and phase changes in turbulent wall-bounded flow. In the statistically steady state that is reached after a long time, the resulting flow exhibits a mean motion of water vapour from the warm wall to the cold wall, where it condenses on average, followed by a net mean mass transfer of droplets from the cold wall to the warm wall.

Key words: condensation/evaporation, drops, turbulence simulation

1. Introduction

Particle-laden turbulent flows can be found in many engineering and natural processes, such as the formation of aerosols, internal combustion in engines, and dispersion of pollution in the atmosphere or in oceans Crowe *et al.* (2011). In the field of multiphase flows, particle-laden turbulent flow remains a challenging topic owing to the dynamic nature of particle motion (dispersed phase), which modulates

†Email address for correspondence: e.russo@tue.nl

the turbulent characteristics of the flow (carrier phase) through two-way coupling. This means not only that the gas affects the particles but also that it is influenced by the particles. In this paper, we focus on differentially heated turbulent channel flow in which the dispersed water droplets have a two-way coupling to the gas flow incorporating, in addition to momentum transfer, heat and mass transfer. The consequences for the overall heat transfer, in terms of the Nusselt number, and for the mass transfer, in terms of the size distribution of the droplets, are studied in detail.

The rapid increase in computing power in the past fifty years has stimulated research into particle-laden turbulent flows. Particle-laden flows are formed by a fluid phase and a solid or liquid phase. The fluid phase is the 'carrier phase' and the solid or liquid phase is the 'dispersed phase' (Mashayek & Pandya 2003). The presence of the dispersed phase requires that the flow around each particle is represented. The most fundamental approach involves full resolution of the flow around each particle. Despite the enormous progress in computing power, it is still impossible to simulate millions of particles interacting with a turbulent flow up to all details of the flow. The computing cost for simulating the flow around each individual particle is prohibitive if a large number of particles is present (Esmaeeli & Tryggvason 1998, 1999; Tryggvason, Scardovelli & Zaleski 2011). Therefore, in the case of turbulent flow with a large number of particles with sizes smaller than the Kolmogorov scale η, it is common practice to adopt a point-particle approach to keep the computational cost at acceptable levels (Elghobashi 1994; Marchioli *et al.* 2008). In this approximation, the motion of a particle is described by the Maxey–Riley equation, which is based on the well-understood physics of low-Reynolds-number flow around a small sphere (Maxey & Riley 1983; Rouson & Eaton 2001; Bec *et al.* 2010). This approach allows numerical simulations with millions of particles (Elghobashi 1991) and has been used to perform direct numerical simulations (DNS) as well as large-eddy simulations (LES) in many applications (Miller & Bellan 2000; Ferrante & Elghobashi 2003; Toschi & Bodenschatz 2009; Balachandar & Eaton 2010).

The coupling between the phases can be classified into three types: (i) 'one-way coupling' if the carrier phase influences the dispersed phase, but the number of particles and the mass loading are too small to have an effect on the carrier phase; (ii) 'two-way coupling' if the dispersed phase has also a noticeable feedback on the flow; and (iii) 'four-way coupling' when the particle concentration is so large that direct particle–particle interaction is important as well. In the simulations presented in this paper, we adopt two-way coupling, characterized by exchange of momentum, heat and mass with the carrier phase. Generally, for the momentum exchange, one must account for the drag force, the body force, the added mass force, the lift force, the pressure drag and the Basset history force. However, the problem can be simplified in the case of a water–air system. According to Armenio & Fiorotto (2001), for particles with a large mass density compared to the fluid mass density, all forces except the Stokes drag force and gravity are negligible.

For point-particle models, the effect of mass and heat transfer in turbulent flows has hardly been addressed. Up to now, only a few studies have been reported on the modelling of heat and mass transfer in a point-particle model that is suitable for numerical computations. In particular, Mashayek (1997) was the first to study evaporating droplet dispersion in homogeneous turbulence with two-way coupling of heat and mass transfer, as well as momentum exchange between droplets and fluid. Miller & Bellan (1999) performed a complete two-way coupled DNS of a temporally developing mixing layer with one stream laden with evaporating hydrocarbon droplets. Later, this approach was extended to a reacting mixing layer (Miller 2001) and to

study the effect of two-way coupling in a spray, including evaporation and combustion phenomena (Mashayek 2000; Reveillon & Vervisch 2005; Wang & Rutland 2005). In a recent work, Masi, Simonin & Bédat (2011) used this approach to generate data for modelling two-phase flows with evaporation using a statistical approach (Mesoscopic Eulerian formalism).

In the present study, we extend the work of Mashayek (1997) and consider wall-bounded turbulent flow with evaporation and condensation using DNS. We consider a channel flow at a frictional Reynolds number of 150 in which one of the walls is heated while the other is being cooled. This leads to a gradient of temperature in the wall-normal direction of the channel and hence also to a non-uniform mean vapour mass fraction. We use a similar point-particle approach for the droplets as Mashayek (1997), but we adopt an incompressible formulation for the carrier phase and restrict ourselves to cases where changes in mass density of the carrier phase due to evaporation and condensation are limited and consistent with a divergence-free velocity field. The governing equations for the point droplets are based on conservation laws and empirical correlations for heat, mass and momentum exchange with the carrier phase.

Moreover, droplet–droplet collisions are ignored because of the small volume fraction considered in our simulations (Elghobashi 1994). In the present model, not all mechanisms present in reality have been incorporated. Droplets can grow unrealistically large and nucleation of droplets is not taken into account. In reality, large droplets will break up if their diameter exceeds a critical value that depends on the local shear rate (Hinze 1956; van Wissen, Schreel & van der Geld 2005). The effect of these limitations on the results is very small. In the simulations presented here, the largest droplet is still only 35 % larger than the initial diameter. Moreover, the relative humidity only slightly exceeds 100 %, so that nucleation does not play a role in the cases considered here.

The aim of this study is to analyse the effects of phase change on the global heat transfer properties of channel flow and on droplet size distribution and motion. In power electronics and microelectronics applications, phase change in microchannels was shown to improve the heat exchange due to the high latent heat of evaporation (Lenert *et al.* 2013). Another way to improve the heat transfer is by employing nanofluids, i.e. a fluid containing nanometre-sized particles. In an earlier study (Kuerten, van der Geld & Geurts 2011), this result was extended to inertial particles in wall-bounded flow. It was found that the presence of a large number of inertial particles significantly increases the effective heat transfer between the channel walls. The particles studied there had the properties of water droplets, but evaporation and condensation were not taken into account. In the present study, we investigate to what extent phase changes affect the heat transfer. This will be quantified by the Nusselt number, which is the non-dimensional ratio of the temperature gradient at the walls and the average temperature gradient over the height of the channel. The Eulerian–Lagrangian model that we adopt allows for the analysis of the effect of heat transport by droplet transport combined with phase change in wall-bounded flow. The change in Nusselt number can be quantified, not only in terms of the change in thermal resistance due to the presence of a dispersed phase, but also by the dynamic effect of droplets undergoing phase change transported in the channel and the heat transport associated with them. In order to distinguish between the different contributions to the Nusselt number, additional simulations with solid particles instead of droplets and without particles altogether will be included in the analysis. Moreover, the influence of the mean gas temperature in the channel, the magnitude of the applied heat flux, the droplet size and volume fraction will be studied.

The simulations are started from a homogeneous droplet distribution and a relative humidity of the carrier gas of 100 %. Initially, the droplets will migrate towards the walls of the channel due to turbophoresis, creating an increase in droplet concentration in the vicinity of the walls. Simultaneously, evaporation and condensation lead to the growth of droplets near the cold wall and shrinkage near the warm wall. This also results in a gradient in water vapour concentration, directed from the cold to the warm wall. In the resulting statistically steady state, the droplet concentration and mean droplet size are approximately constant. In that situation, diffusion and turbulent dispersion of water vapour will lead to a mean flux of water vapour from the warm to the cold wall. Conservation of water mass shows that this must be compensated for by a net mass flux of water droplets from the cold to the warm wall. We will analyse the time needed before this equilibrium state is reached and quantify the magnitude of these mass fluxes. To the best of our knowledge, this is the first time that such a water cycle has been studied in a numerical simulation.

The paper is organized as follows. In § 2, we introduce the governing equations for the air–water vapour carrier phase and the dispersed droplet phase. Section 3 is devoted to a description of the numerical method and the specifications of the simulations presented in this paper. In § 4, we will present and analyse the results of the simulations and, in particular, address the effects of the evaporating and condensing droplets on the heat transfer between the walls of the channel and the inhomogeneity of droplet size in the wall-normal direction of the channel. In § 5, the turbulence modulation by evaporating droplets is analysed. Finally, § 6 is devoted to concluding remarks.

2. Governing equations

In this section, governing equations for the carrier phase and for the droplets are presented, including the models for momentum, heat and mass transfer between the two phases. We consider a mixture of air and water vapour, and refer to this carrier phase as the 'gas' in the sequel, while the dispersed phase consists of water droplets. Henceforth, the terms 'droplet' and 'particle' will refer to water droplet and solid particle, respectively. A particle does not exchange mass with the carrier phase, only energy and momentum. We will first present the equations for the gas phase and then those for the droplets. Since the equations for the gas phase contain coupling terms that depend on the properties of the droplets, we will postpone the specification of these coupling terms to the final part of this section.

2.1. *Gas*

The gas is considered in an Eulerian way and is assumed to behave as an incompressible fluid. This means that the gas mass density is constant, $\rho_g = \text{const}$. However, it does not mean that the mass densities of air (ρ_a) and water vapour (ρ_v) cannot vary. Indeed, both are functions of position $\boldsymbol{x}$ and time t, $\rho_g = \rho_a(\boldsymbol{x}, t) + \rho_v(\boldsymbol{x}, t) = \text{const}$.

In the problems we investigate, the incompressibility assumption is justified for the following reasons:

(i) The Mach number is much smaller than one.

(ii) The change in mass density due to changes in temperature is of the order of 2 % or less.

(iii) In all simulations, the gas is initially saturated, with 100 % relative humidity everywhere. When the simulation starts, the channel is differentially heated in such a way that the amount of water vapour condensing in the colder part of the channel is balanced by evaporation of droplets in the warmer part.

In view of the assumed incompressibility, ρ_a and ρ_v vary in time and space during the transient phase, but their sum remains constant, which means that local variations of air mass density are balanced by local variations of water mass density, and the same for local variations in time:

$$\boldsymbol{\nabla}\rho_a = -\boldsymbol{\nabla}\rho_v \quad \text{and} \quad \frac{\partial \rho_a}{\partial t} = -\frac{\partial \rho_v}{\partial t}. \tag{2.1a,b}$$

The model for the motion of the gas consists of the continuity equation for incompressible flow, which implies a divergence-free flow,

$$\boldsymbol{\nabla}\cdot\boldsymbol{u} = 0, \tag{2.2}$$

and the Navier–Stokes equations for momentum conservation. We adopt the Navier–Stokes equation in rotational form,

$$\frac{\partial \boldsymbol{u}}{\partial t} + \omega \times \boldsymbol{u} + \boldsymbol{\nabla} P = \nu \Delta \boldsymbol{u} + \frac{\boldsymbol{F}}{\rho_g} + \frac{\mathscr{L}_{\boldsymbol{u}}}{\rho_g}, \tag{2.3}$$

following Kuerten (2006). In (2.3), $\omega = \boldsymbol{\nabla}\times\boldsymbol{u}$ is the vorticity, $P = p/\rho_g + \frac{1}{2}\boldsymbol{u}^2$, ν is the kinematic viscosity of the gas, p is the static pressure, ρ_g is the gas mass density, and $\boldsymbol{F}$ is the driving force necessary to maintain a constant total mass flow rate. Finally, $\mathscr{L}_{\boldsymbol{u}}$ is the term describing the momentum exchange between the two phases, which will be specified in § 2.3.

The water vapour is also treated in an Eulerian way. The rate of change of the vapour mass density is expressed as the sum of transport due to diffusion, convection and mass transfer between the two phases by evaporation and condensation:

$$\frac{\partial \rho_v}{\partial t} + \boldsymbol{\nabla}\cdot(\rho_v \boldsymbol{u}) - \boldsymbol{\nabla}\cdot(\mathscr{D}\boldsymbol{\nabla}\rho_v) = \mathscr{L}_v. \tag{2.4}$$

The term $\mathscr{L}_v$ represents the mass transfer between the droplets and the water vapour, which will be specified in § 2.3. We are dealing with a binary system of air and water vapour for which a single diffusion coefficient $\mathscr{D}$ is adequate to represent the diffusion of one species into the other (Bird, Stewart & Lightfoot 1960, p. 502). This diffusion coefficient is assumed to be constant in space and time, which is motivated by the fact that the solute (water vapour) is present at a much lower concentration than the solvent (air). Hence, under all simulated conditions, the diffusion of water vapour in dry air will determine the diffusion coefficient $\mathscr{D}$. Moreover, the variations in temperature in all simulations are sufficiently small to use a constant value of $\mathscr{D}$.

The temperature equation is obtained from the equation expressing the conservation of internal energy of the two phases. The total internal energy E in a volume ΔV can be written as the sum of the integral of the internal energy density of the gas phase over the volume and the internal energy of all droplets contained in the volume:

$$E = \int_{\Delta V} [(\rho_a c_{v,a} + \rho_v c_{v,v}) T_g + \rho_v \ell_0] \,\mathrm{d}V + \sum_{i=1}^{N_\Delta} E_i. \tag{2.5}$$

Here ρ_a (ρ_v) and $c_{v,a}$ ($c_{v,v}$) are the mass density and specific heat capacity at constant volume of the air (vapour) respectively, ℓ_0 is the latent heat of water at $T = 0\,^\circ\mathrm{C}$ and T_g is the gas temperature. Moreover, N_Δ is the number of droplets present within ΔV

and E_i is the internal energy of droplet i. The specific heat capacities are assumed to be independent of temperature. This is an accurate assumption in the temperature range considered in this paper, since the specific heat capacities of water and air vary less than 0.1 % in the temperature range of each simulation.

In this work, we will disregard the contribution of the kinetic energy to the total energy and the work performed by the driving force and by the viscous force. This is justified since the contribution from kinetic energy is very small (at the typical bulk velocity of 1 m s^{-1} that we consider) compared to the internal energy. If all kinetic energy in the system were to be converted into internal energy, the increase in temperature would only be approximately 5×10^{-4} °C. Conservation of energy is incorporated by equating the rate of change of the energy E in ΔV to the change in energy through the boundaries of the volume due to convection and due to heat conduction and diffusion of vapour. After application of Gauss's divergence theorem, this leads to

$$\frac{\partial}{\partial t}[(\rho_a c_{v,a} + \rho_v c_{v,v})T_g + \rho_v \ell_0] + \boldsymbol{\nabla} \cdot [((\rho_a c_{v,a} + \rho_v c_{v,v})T_g + \rho_v \ell_0)\boldsymbol{u}] = \boldsymbol{\nabla} \cdot (k_g \boldsymbol{\nabla} T_g) + \boldsymbol{\nabla} \cdot [((c_{p,v} - c_{p,a})(T_g - T_{\ell_0}) + \ell_0)\mathscr{D} \boldsymbol{\nabla} \rho_v] + \mathscr{L}_E. \tag{2.6}$$

The terms on the left-hand side represent the rate of change of internal energy and the convection of internal energy. The first term on the right-hand side is the change in internal energy by heat conduction, where we denote the heat conductivity coefficient of the gas by k_g. The second term on the right-hand side represents diffusion arising from variation in composition, which is the dominant diffusion mechanism in the case of a water–air system under not so extreme conditions in terms of temperature and pressure (a review is given in Bird *et al.* (1960)). Pressure and temperature gradients are sufficiently small to ignore pressure diffusion and thermal diffusion in this paper (Bird *et al.* 1960, p. 566). The quantities $c_{p,a}$ and $c_{p,v}$ denote the specific heat capacities of air and vapour at constant pressure. The quantity $(T_g - T_{\ell_0})$ is the difference between the gas temperature and the temperature at which the latent heat is evaluated (273.15 K). The last term on the right-hand side describes the internal energy transfer between the two phases and will be specified below.

Next, substitution of (2.4) and the use of (2.1) and (2.2) results in the following governing equation for the gas temperature:

$$(\rho_a c_{v,a} + \rho_v c_{v,v}) \left(\frac{\partial T_g}{\partial t} + \boldsymbol{\nabla} \cdot (\boldsymbol{u} T_g) \right) = k_g \nabla^2 T_g + \mathscr{L}_{wd} + \mathscr{L}_{diff} + \mathscr{L}_{2way}. \tag{2.7}$$

Although, individually, k_g and $(\rho_a c_{v,a} + \rho_v c_{v,v})$ are functions of the binary mixture composition, we assume that the heat diffusivity $k_g/(\rho_a c_{v,a} + \rho_v c_{v,v})$ in (2.7) is constant. For the small values of the vapour mass fraction considered here, this assumption appears to be accurate (Turns 2006). Note, however, that the dependence of k_g on ρ_v is taken into account in the term $\mathscr{L}_{wd}$ in (2.7), which represents the transport of energy due to diffusion of water vapour and due to the dependence of the thermal conductivity of the gas on the vapour mass density:

$$\mathscr{L}_{wd} = \left\{ \frac{\partial k_g}{\partial \rho_v} + \mathscr{D}(c_{p,v} - c_{p,a}) \right\} \boldsymbol{\nabla} \rho_v \cdot \boldsymbol{\nabla} T_g. \tag{2.8}$$

Here, we use $\boldsymbol{\nabla} k_g = (\partial k_g / \partial \rho_v) \boldsymbol{\nabla} \rho_v$. The third term on the right-hand side is the contribution to the temperature change from diffusion of vapour and is equal to

$$\mathscr{L}_{diff} = (R_a - R_v)\mathscr{D}(T_g - T_{\ell_0})\nabla^2 \rho_v, \tag{2.9}$$

where $R_a = c_{p,a} - c_{v,a}$ is the specific gas constant of air and, similarly, $R_v = c_{p,v} - c_{v,v}$ is the specific gas constant of vapour. Finally,

$$\mathscr{L}_{2way} = \mathscr{L}_E - ((c_{v,v} - c_{v,a})T_g + \ell_0)\mathscr{L}_v \tag{2.10}$$

represents the contribution from the coupling between the two phases, which will be specified in § 2.3.

The time evolution of the gas velocity, gas pressure, gas temperature and water vapour mass density can be calculated from (2.2), (2.3), (2.7) and (2.4). The two-way coupling terms in these equations will be specified after the presentation of the governing equations for the droplets.

2.2. *Droplets*

In this subsection, the equations of motion, mass and temperature of the droplets are presented. The droplets are considered in a Lagrangian way. The point-particle approach is used, implying that we also assume the droplets to have uniform temperature. The ratio of the heat transfer resistances inside and at the surface of a droplet can be quantified by the Biot number, which is defined as $Bi = h_m R/k_l$, with h_m the convective heat transfer coefficient from gas to droplet, R the typical radius of a droplet and k_l the thermal conductivity of the droplet. For the small droplets that we consider here, the convective heat transfer coefficient equals $h_m = k_g/R$, with k_g the thermal conductivity of the carrier gas. Therefore, the typical value of the Biot number is equal to the ratio of the thermal conductivities of water and the carrier gas: $Bi = 0.046$. This indicates that the typical time scale of heat conduction inside a droplet is more than 20 times larger than the typical time scale for heat transfer from the carrier gas to a droplet. Therefore, the assumption of uniform droplet temperature is justified.

Since the droplets are small and have a much higher mass density than the gas, the drag force is the dominant force exerted by the gas on a droplet (Armenio & Fiorotto 2001). We do not take gravity into account, but it may be added in the spanwise direction to reproduce a real test case. However, the settling of droplets is not a focal point in this study. Therefore, Newton's law applied to a droplet can be written as

$$\frac{\mathrm{d}(m_i \boldsymbol{v}_i)}{\mathrm{d}t} = m_i(\boldsymbol{u}(\boldsymbol{x}_i, t) - \boldsymbol{v}_i)\frac{(1 + 0.15Re_p^{0.687})}{\tau_p} + \boldsymbol{v}(\boldsymbol{x}_i, t)\frac{\mathrm{d}m_i}{\mathrm{d}t}. \tag{2.11}$$

Here, m_i is the mass of particle i, $\boldsymbol{v}_i$ is its velocity and τ_p is the droplet relaxation time given by $\tau_p = \rho_l d_i^2/(18\mu_g)$. Moreover, $Re_p = |\boldsymbol{v}_i - \boldsymbol{u}(\boldsymbol{x}_i, t)|d_i/\nu$ is the Reynolds number based on the droplet diameter d_i and the relative velocity between the droplet and the carrier gas at the droplet position, ρ_l is the mass density of liquid water and μ_g is the dynamic viscosity of the gas. The two terms on the right-hand side are the drag force, where the standard Schiller–Naumann drag correlation valid for droplet Reynolds numbers between 0 and 1000 is adopted (Clift, Grace & Weber 1978), and the change in momentum due to phase change. Equation (2.11) can also be written in terms of accelerations, yielding the following droplet equation of motion:

$$\frac{\mathrm{d}\boldsymbol{v}_i}{\mathrm{d}t} = (\boldsymbol{u}(\boldsymbol{x}_i, t) - \boldsymbol{v}_i)\frac{(1 + 0.15Re_p^{0.687})}{\tau_p}. \tag{2.12}$$

The Lagrangian droplet tracking requires integrating the trajectory equation:

$$\frac{\mathrm{d}\boldsymbol{x}_i(t)}{\mathrm{d}t} = \boldsymbol{v}_i, \tag{2.13}$$

in which the particle velocity $\boldsymbol{v}_i$ is computed from (2.12).

In order to derive an equation for the droplet temperature that takes into account the heat and mass transfer to and from the gas, we consider the rate of change of the internal energy of a droplet:

$$\frac{\mathrm{d}E_i}{\mathrm{d}t} = \frac{\mathrm{d}}{\mathrm{d}t}(m_i c_l T_i) = h_v \frac{\mathrm{d}m_i}{\mathrm{d}t} + h_m A_i (T_g(\boldsymbol{x}_i, t) - T_i). \tag{2.14}$$

This equation states that the variation of the internal energy of droplet i is due to contributions from condensation and evaporation, which change the mass of the droplet, and due to heat exchanged by convection at the droplet surface. The heat exchange at the droplet surface is modelled using the heat transfer coefficient h_m as defined by Bird *et al.* (1960). In a single droplet context, the relevant temperature difference for convection is that between the surroundings and the droplet surface temperature. In (2.14), the surface temperature is the same as the droplet temperature because we assume the droplet temperature to be homogeneous. The temperature of the surroundings is taken as the temperature of the gas $T_g(\boldsymbol{x}_i, t)$ at the location of droplet i. Finally, A_i is the surface area of droplet i. Kinetic energy is not included here because it is much smaller than the internal energy: the kinetic energy of a droplet with a velocity of the order of 1 m s^{-1} is less than 0.05 % of its internal energy. In the first term on the right-hand side, h_v denotes the specific enthalpy of water vapour. Denoting the specific enthalpy of water as h_l and the droplet volume by V_i, (2.14) can be rewritten as

$$\rho_l c_l V_i \frac{\mathrm{d}T_i}{\mathrm{d}t} = (h_v - h_l)\frac{\mathrm{d}m_i}{\mathrm{d}t} + h_m A_i (T_g(\boldsymbol{x}_i, t) - T_i). \tag{2.15}$$

Here, we used $h_l = c_l T$ and chose the zero point of enthalpy at $T = 0\,^{\circ}\mathrm{C}$ in the liquid water phase: $h_l(T = 0\,^{\circ}\mathrm{C}) = 0$. Therefore, the water vapour enthalpy is

$$h_v = h_v(T = 0\,^{\circ}\mathrm{C}) + c_{p,v} T_i = h_l(T = 0\,^{\circ}\mathrm{C}) + \ell_0 + c_{p,v} T_i = \ell_0 + c_{p,v} T_i. \tag{2.16}$$

To close (2.15), we need to express h_m and $\mathrm{d}m_i/\mathrm{d}t$ in terms of known quantities. We use correlations from the literature that are applicable to spherical droplets in the range of Reynolds and Prandtl numbers relevant to our simulations. For forced convection around a sphere, the heat-transfer correlation is chosen as (Bird *et al.* 1960)

$$\frac{h_m d_i}{k_g} = 2 + 0.6 Re_p^{1/2} Pr^{1/3}, \tag{2.17}$$

where Pr is the Prandtl number of the carrier gas.

For the mass transfer, we also follow Bird *et al.* (1960), who considered condensation of a hot vapour on a cold surface in the presence of a non-condensable gas. This is applicable in the situation that we consider here, since the carrier gas consists of a mixture of water vapour, which is condensable, and the non-condensable air. The resulting expression for the mass transfer is

$$\frac{\mathrm{d}m_i}{\mathrm{d}t} = -\frac{m_i Sh}{3\tau_p Sc} \ln\left(\frac{1 - x_{v,\delta}}{1 - x_{v,0}}\right), \tag{2.18}$$

where the Schmidt number $Sc = \mu_g/(\rho_g \mathscr{D})$, and $x_{v,\delta}$ and $x_{v,0}$ are the vapour mass fractions ($x_v = \rho_v/\rho_g$) in the surroundings of the droplet and at the surface of the droplet, respectively. The Sherwood number is given by $Sh = 2 + 0.6Re_p^{1/2}Sc^{1/3}$ (Bird *et al.* 1960).

The driving quantity in (2.18) is the difference $x_{v,\delta} - x_{v,0}$. Since interfacial resistance is negligible at the droplet surface, we can assume that the air at the droplet surface is saturated (Popov 2005; Siregar & Kuerten 2013). Therefore, with the ideal gas law, $x_{v,0}$ can be written in terms of the particle temperature T_i and the saturation pressure $p_{v,sat}$ on the droplet surface as

$$x_{v,0} = \frac{\rho_{v,sat}}{\rho_g} = \frac{p_{v,sat}}{R_v T_i \rho_g}, \tag{2.19}$$

where R_v is the specific gas constant of water vapour. The saturation pressure is calculated using Antoine's relation (Antoine 1888),

$$\frac{p_{v,sat}(T_i)}{p_{ref}} = \exp\left(A - \frac{B}{C + T_i}\right), \tag{2.20}$$

where T_i is in degrees Celsius, p_{ref} is the reference pressure of 10^5 Pa, and the coefficients are $A = 11.6834$, $B = 3816.44\,^\circ\mathrm{C}$ and $C = 226.87\,^\circ\mathrm{C}$. For $x_{v,\delta}$, we take the vapour mass fraction of the gas at the position of the droplet, $\rho_v(\boldsymbol{x}_i, t)$.

The time evolution of particle velocity, position, temperature and mass can be calculated from (2.12), (2.13), (2.15) and (2.18). In the next section, the two-way coupling terms between the gas phase and the droplets will be specified.

2.3. *Coupling terms*

The two-way coupling terms in the governing equations for the gas phase satisfy the requirement that these terms do not change the total water mass, total momentum and total internal energy in the system. They only transfer mass, momentum and internal energy from one phase to the other. Moreover, we will assume that the two-way coupling terms act as a point force in the governing equations for the gas.

Based on these two considerations, the two-way coupling term in the Navier–Stokes equation for the gas phase (2.3) can be written as

$$\mathscr{L}_{\boldsymbol{u}} = -\sum_{i=1}^{N} \frac{\mathrm{d}(m_i \boldsymbol{v}_i)}{\mathrm{d}t}\delta(\boldsymbol{x} - \boldsymbol{x}_i) = -\sum_{i=1}^{N} m_i \frac{\mathrm{d}\boldsymbol{v}_i}{\mathrm{d}t}\delta(\boldsymbol{x} - \boldsymbol{x}_i) - \sum_{i=1}^{N} \boldsymbol{v}_i \frac{\mathrm{d}m_i}{\mathrm{d}t}\delta(\boldsymbol{x} - \boldsymbol{x}_i). \tag{2.21}$$

The coupling term is split into two contributions representing the momentum transfer from the droplet to the gas due to acceleration and that due to mass transfer arising from evaporation or condensation, respectively. The delta-function, $\delta(\boldsymbol{x} - \boldsymbol{x}_i)$, indicates that the coupling terms only act at the locations of the droplets.

The two-way coupling term in the water vapour equation (2.4) follows from conservation of water mass and is given by

$$\mathscr{L}_v = -\sum_{i=1}^{N} \frac{\mathrm{d}m_i}{\mathrm{d}t}\delta(\boldsymbol{x} - \boldsymbol{x}_i). \tag{2.22}$$

The two-way coupling term in the gas temperature equation (2.7) follows from conservation of internal energy and using (2.15) for the change in particle temperature can be written as

$$\begin{aligned}\mathscr{L}_{2way} &= -\sum_{i=1}^{N}[c_{p,v}T_i + (c_{v,a} - c_{v,v})T_g]\frac{\mathrm{d}m_i}{\mathrm{d}t}\delta(\boldsymbol{x} - \boldsymbol{x}_i) - \sum_{i=1}^{N} h_m A_i (T_g - T_i)\delta(\boldsymbol{x} - \boldsymbol{x}_i) \\ &= \mathscr{L}_{evap} + \mathscr{L}_{conv}, \end{aligned} \tag{2.23}$$

where $\mathscr{L}_{evap}$ and $\mathscr{L}_{conv}$ represent the gain (loss) of energy for the carrier phase due to evaporation (condensation) of the droplets, and the convective heat transfer between fluid and droplets, respectively.

In the next section, the numerical method will be described, including the way in which the coupling terms are evaluated in the numerical method.

3. Numerical method and set-up of the simulations

In this section, we first sketch the main elements of the numerical approach and pay special attention to the coupling between the discrete droplet phase and the continuous gas phase. Next, the geometry of the channel and the applied boundary conditions are described. Then, the parameters and initial conditions used in the simulations are presented.

The proposed model for two-way coupling in droplet-laden turbulent flow is applied in DNS of turbulent channel flow. First, the numerical method adopted for the continuous phase is described and, after, that for the droplets. Finally, the method for treating the coupling terms numerically is discussed.

DNS of turbulent channel flow is performed using an extended version of the pseudo-spectral code as described in Kuerten (2006). The extensions consist of the incorporation of equations for the water vapour mass density and for the temperature and of two-way coupling of momentum, vapour mass and internal energy between the gas and the droplet phase. The application of periodic boundary conditions in the streamwise and spanwise directions allows the use of a Fourier–Galerkin approach, whereas, in the wall-normal direction, a Chebyshev collocation method is used. The time integration method for the gas consists of a combination of a third-order accurate compact-storage explicit Runge–Kutta method for the nonlinear terms (including the coupling terms) and the implicit Crank–Nicolson method for the viscous and pressure terms. The nonlinear terms are computed in physical space using fast Fourier transform and the 3/2 rule to prevent aliasing errors. The velocity field is divergence-free within machine accuracy by applying the influence matrix method. For further details concerning this spectral method for the gas phase, see Kuerten (2006).

The time integration of the gas phase requires that the coupling terms are computed at the same times as the other terms in the governing equations of the gas phase. Since, apart from a minus sign, the same coupling terms are needed in the equations for the droplets as in the equations for the gas phase, the same Runge–Kutta method is applied to the governing equations of the droplets. The gas properties (velocity, temperature and vapour mass density) at the droplet location are calculated by second-order accurate tri-linear interpolation. It is known from the literature that a fourth-order interpolation in DNS leads to negligible differences in the statistical particle properties (Marchioli *et al.* 2008).

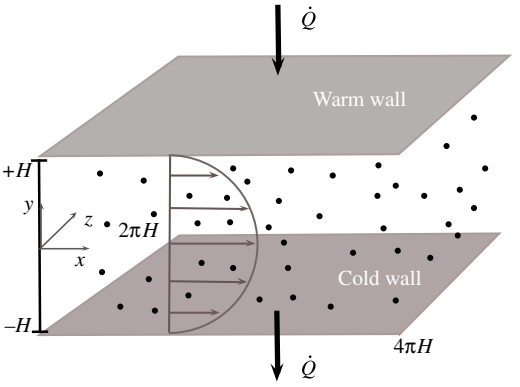

FIGURE 1. Channel geometry.

The coupling terms of each droplet are computed at the droplet location and successively distributed to the eight surrounding mesh points using the same weights as used for the tri-linear interpolation of the gas properties at the droplet positions. This means that, in this numerical formulation, the delta-function $\delta(\boldsymbol{x} - \boldsymbol{x}_i)$ is implemented in such a way that the transfer is spread over the eight grid points neighbouring the droplet. Subsequently, the two-way coupling terms resulting from the contributions of all droplets are added to the nonlinear terms in the gas equations in physical space and transformed to Fourier space. If only a few droplets are present, this way of calculating the coupling terms may lead to numerical oscillations. However, the contributions to high wavenumbers caused by the delta-function are, for a large part, cancelled if the number of droplets is of the same order as the number of grid points, as in the simulations reported here (Kuerten *et al.* 2011).

The domain has a size of $4\pi H$ in the streamwise direction and $2\pi H$ in the spanwise direction, where H is half the channel height (see figure 1). For the streamwise, wall-normal and spanwise directions, the notation x, y and z is used, respectively. In both homogeneous directions (spanwise and streamwise), 128 Fourier modes are used and 129 Chebyshev collocation points are employed in the wall-normal direction. The grid points are clustered near the walls in order to resolve the boundary layer. Periodic boundary conditions are applied in the streamwise and spanwise directions and the no-slip condition is adopted at the walls. On the upper (warm) wall, a uniform and constant heat flux is supplied to the channel, which is equal to the heat flux extracted from the lower (cold) wall in order to conserve the total thermal energy of the system. For the droplets, periodic conditions are applied in the homogeneous flow directions, which means that, when a droplet leaves the domain in one of these directions, it re-enters the domain from the other side with the same properties. If a droplet approaches a wall within a distance of its radius, rules of elastic collision of a hard spherical particle are applied without heat transfer.

Simulations are performed at a frictional Reynolds number of approximately $Re_\tau = 150$, based on friction velocity $u_\tau = \sqrt{\tau_w/\rho_g}$ and half the channel height, where $\tau_w = \mu_g(\partial\langle u\rangle/\partial y)|_{y=\pm H}$ is the wall shear stress and $\langle u\rangle$ the mean streamwise velocity component averaged over the two homogeneous directions and time. Marchioli *et al.* (2008) also show that the flow at this Reynolds number has reached a state of fully developed turbulence. The gas parameters are computed using a mass-density weighted average according to the dry air and water vapour concentrations. The droplets or

Case	Particles	Initial temperature (°C)	Heat flux (W m^{-2})
Reference	Water droplets	20	32
High temperature	Water droplets	50	34
High heat flux	Water droplets	20	160
Bigger droplets	Water droplets	20	32
Smaller volume fraction	Water droplets	20	32
Solid	Solid particles	20	32
No particles	—	20	32

TABLE 1. Definition of the test cases.

solid particles have an initial diameter $d_i/H = 3.09 \times 10^{-3}$, which corresponds to a Stokes number of $St = \tau_p^+ = \tau_p u_\tau^2/\nu = 10$. This initial droplet size ensures that, during the simulation, the size of growing particles near the cold wall does not exceed the Kolmogorov length. On the other hand, smaller particles would result in an attenuated turbophoresis effect, especially in the warm part of the channel where evaporation occurs. There are two million droplets or particles, which are initially randomly and homogeneously distributed over the channel domain. The initial volume fraction is approximately 2.2×10^{-4}, which is in the range where droplet–droplet collisions can be ignored but two-way coupling is relevant (Elghobashi 1994). During the simulation, particles are clustered near the walls due to turbophoresis. Here, the two-way coupling formulation still remains valid although the local particle concentration is very close to the upper bound of the two-way coupling regime. The initial droplet velocity and temperature are equal to the gas velocity and temperature at the droplet location.

The flow is initialized by a turbulent velocity field in the statistically steady state of fully developed turbulence obtained from a simulation without droplets at the same Reynolds and Prandtl numbers. The initial temperature is homogeneous and, when the simulation starts, a constant heat flux is imposed at both walls to gradually generate a temperature gradient in the wall-normal direction. The magnitude of the heat flux is shown in table 1. On the upper wall, the heat flux is positive, while it is negative on the lower wall. The initial relative humidity ϕ, which is the ratio of the partial water vapour pressure and the saturation pressure, equals 100 % all over the channel. Hence, the air–vapour mixture is saturated. It is noted that this relative humidity equals $\rho_v T_g(\boldsymbol{x})/\rho_{v,sat} T_i(\boldsymbol{x})$ and, apart from the initial condition, is therefore not equal to the normal relative humidity, which is assessed at identical temperatures: $\rho_v T_g(\boldsymbol{x})/\rho_{v,sat} T_g(\boldsymbol{x})$. In the initial transient phase, the temperature changes because of the applied thermal boundary conditions. Consequently, the saturation conditions change according to the local change of the temperature. The applied heat fluxes lead to evaporation of droplets in the upper half of the channel (warmer part), while condensation will occur in the lower half (colder part). Using these settings, we simulate an experiment in which an initially isothermal channel flow with droplets is heated at the top wall and cooled at the bottom wall.

We investigated seven test cases as described in table 1. In the reference test case, the initial temperature is 20 °C; hereafter we refer to this case as 'reference'. The case named 'solid' is identical to 'reference' but the droplets are replaced by solid particles so that phase transition between the gas and particle phases is not possible. The case 'no particles' uses the same settings for the boundary conditions and flow parameters but is without particles. The two cases named 'high temperature' and

'high heat flux' serve to investigate the effects of different physical conditions. In the 'high temperature' case, the initial temperature is increased from 20 to 50 °C, while, in the 'high heat flux' case, the heat flux applied at the walls is five times higher than in the reference case. In the 'bigger droplets' case, the droplet diameter is twice as big as in the other simulations, corresponding to a Stokes number equal to 40. Finally, the effect of the volume fraction is investigated in the 'smaller volume fraction' case using half the volume fraction of the reference case.

4. Analysis of the effect of phase transition of droplets on turbulent heat transfer

In this section, the simulation results of the test cases will be presented and analysed. In test cases with water droplets, several phenomena play a role. The heat flux applied at both walls leads to a non-uniform temperature profile in the wall-normal direction. Near the warm wall, droplets will evaporate and, near the cold wall, water vapour will condense. In this way, a non-uniform water vapour concentration will arise, which leads, on average, to a transport of vapour from the warm to the cold wall. On a larger time scale, the inhomogeneity of the turbulence in the wall-normal direction leads to turbophoresis, through which droplets will move, on average, from the centre of the channel towards the walls, where the temperature and, hence, the mean droplet size attain different values. This, together with the turbulent motion of droplets, will lead to a gradually increasing variance of droplet size. In this section, we will first study the thermal properties of the flow and, in particular, focus on the heat transfer between the walls quantified by the Nusselt number. Next, we will consider the droplet size and investigate the mean transport of water including both droplets and vapour.

In the analysis presented in this section, we make use of quantities averaged over the homogeneous directions. This averaging is denoted by a bar over the corresponding variable. When considering the statistically steady state, we also average over time. Quantities averaged over the two homogeneous directions and time are denoted by brackets, $\langle\cdot\rangle$. We distinguish between gas quantities and quantities of the dispersed phase. The gas quantities are known in all Chebyshev collocation points and averaging over homogeneous directions can be easily performed both in Fourier space and in real space (Eulerian averaging). Quantities of the dispersed phase are only known at the locations of the droplets or particles. Averages over homogeneous directions of the dispersed phase are computed by averaging over all droplets that at some time are contained in a slab parallel to the channel walls (Lagrangian averaging). Specifically, we divide the channel into uniformly spaced bins in the wall-normal direction and compute the average profiles using these bins. We use 40 bins, since that number is sufficiently large to accurately represent the dependence of the statistical quantities on the wall-normal coordinate and sufficiently small to minimize statistical errors arising from a too small number of particles in one bin. For the computation of statistical properties of the two-way coupling terms in the gas equations and the relative temperature between particles and carrier gas, the bins defined by the Chebyshev collocation points are used in order to obtain these quantities at the same points as the other statistical properties of the carrier gas. It should be noted that, due to their size, no particles can be present in the first two grid cells neighbouring both walls. Therefore, two-way coupling terms equal zero there. Since droplets can have an arbitrary size, small droplets could be present in these cells, but, in the simulations reported here, this has not been observed.

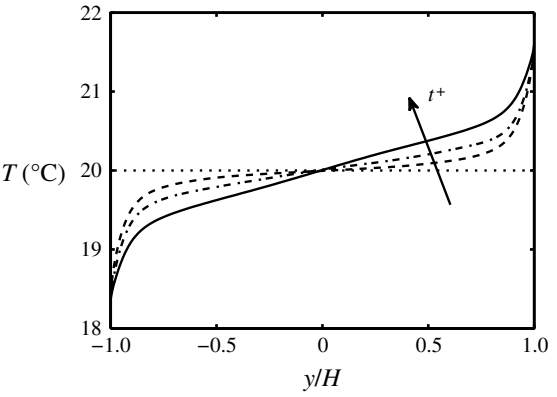

FIGURE 2. Reference case. Mean gas temperature as a function of the wall-normal coordinate at several instants of time: $t^+ = 0$ (·····); $t^+ = 400$ (– – –); $t^+ = 800$ (–·–); averaged over a long time interval in the statistically steady state for temperature, $5000 < t^+ < 16\,000$ (——).

4.1. *Thermal properties*

We consider a channel flow in which we impose a constant heat flux at the walls. This creates a temperature gradient in the wall-normal direction, which leads to evaporation (condensation) in warmer (colder) regions, since, initially, the air is saturated. In figure 2, the fluid temperature of the reference case is shown, averaged over the homogeneous directions, as a function of the normalized wall-normal coordinate y/H at several instances in time (t^+ is the dimensionless time $t^+ = tu_\tau^2/\nu$). The figure shows the development of an inhomogeneous temperature profile from the uniform initial temperature. A steady temperature profile is reached around $t^+ = 5000$, after which the mean temperature exhibits only small fluctuations around the steady profile. As a consequence of evaporation and condensation induced by the changing temperature, the mean water vapour mass fraction changes in time, as figure 3 shows. An inhomogeneous water vapour concentration profile in the wall-normal direction is seen to develop, which closely resembles the mean temperature profile. Also, for the water vapour concentration, a steady profile is reached around $t^+ = 5000$.

In the statistically steady state, the difference in temperature between the channel walls depends considerably on whether or not there are particles present in the flow and whether or not the particles can undergo phase change. This is illustrated by a comparison of the reference case (with water droplets) with the case with solid particles and with the case without particles. The initial and boundary conditions are the same for the three cases and the properties of the solid particles are the same as those of the water droplets, with the exception that no evaporation or condensation can occur. Figure 4 shows the mean temperature profiles for these three cases as functions of the wall-normal coordinate in the statistically steady state. It can be seen that the presence of particles has an influence on the heat transfer properties of the channel, which is in agreement with the results shown in Kuerten *et al.* (2011). The temperature difference between the walls reduces considerably when solid particles are added to a clean single-phase flow. Adding droplets instead of solid particles gives rise to an even larger decrease in the temperature difference between the walls.

In order to understand the reason for the reduced temperature difference when droplets are added instead of particles, we focus on the region close to the upper,

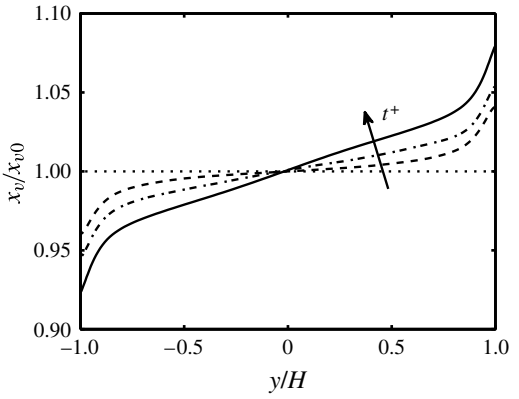

FIGURE 3. Reference case. Vapour mass density normalized by its uniform initial value as a function of the wall-normal coordinate at several instants of time: $t^+ = 0$ (·····); $t^+ = 400$ (– – –); $t^+ = 800$ (–·–); averaged over a long time interval in the statistically steady state for vapour mass density, $5000 < t^+ < 16\,000$ (——).

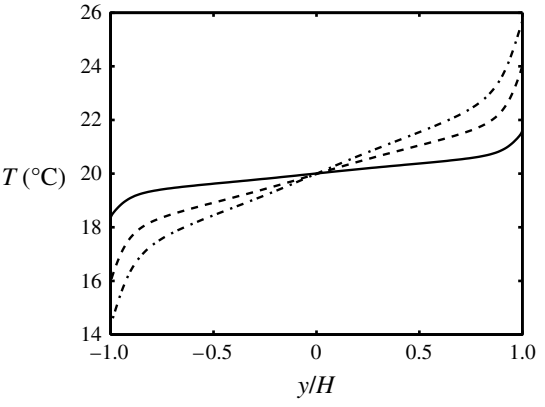

FIGURE 4. Mean gas temperature in the statistically steady state (averaged over $5000 < t^+ < 16\,000$): reference case with water droplets (——); with solid particles (– – –); no particles (–·–).

warm wall. Similar arguments apply to the lower, cold wall. We will first identify the terms in the equation for the temperature of the carrier gas that play an important role in the near-wall region. Then, we will explain the sign of these terms and compare their magnitude for the reference, solid and no particles cases. Finally, we will use this to understand the difference in temperature evolution between the three cases.

Figure 5 shows the temperature histories at the warm wall for the three cases: reference, solid and no particles. The different temperature response seen in the three cases starts in the early stages of the transient phase. Since, at $t^+ \approx 30$, the difference between solid and no particles is easily visible, we analyse the terms in the energy equation (2.7) at this time. Figure 6 shows the magnitude of the terms in the energy equation, averaged over the homogeneous directions, in the region close to the warm wall for the reference case. We distinguish the gas convection term $(-(\rho_a c_{v,a} + \rho_v c_{v,v})\boldsymbol{\nabla} \cdot (\boldsymbol{u} T_g))$, the thermal diffusion term $(k_g \nabla^2 T_g)$, the two-way coupling term due to phase change $(\mathscr{L}_{evap})$, the two-way coupling term due to

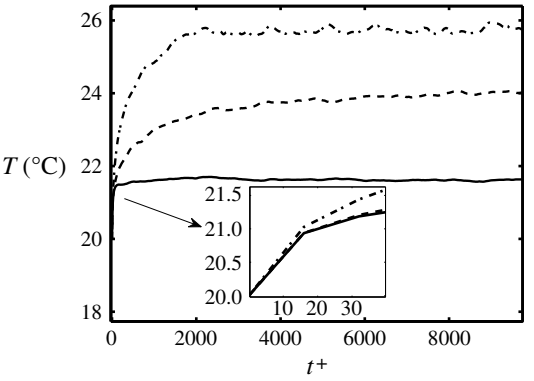

FIGURE 5. Mean temperature history of the warm wall: reference case with water droplets (——); solid particles (– – –); no particles (–·–).

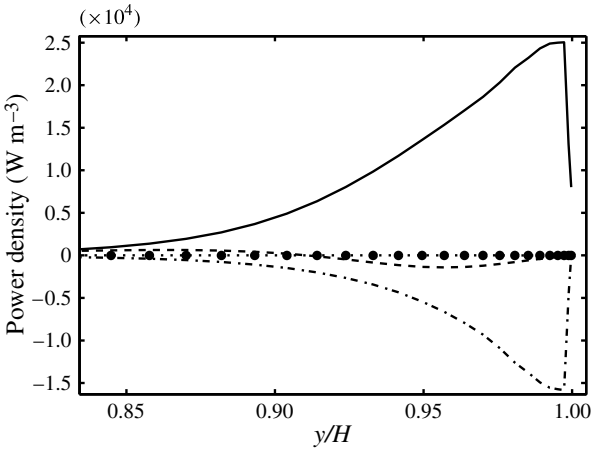

FIGURE 6. Terms in the energy equations for the reference case as a function of the wall-normal coordinate close to the warm wall at $t^+ = 32$: diffusion term $k_g \nabla^2 T_g$ (——); gas convection term $-(\rho_a c_{v,a} + \rho_v c_{v,v}) \boldsymbol{\nabla} \cdot (\boldsymbol{u} T_g)$ (– – –); convective flux coupling term $\mathscr{L}_{conv}$ (–·–); evaporation coupling terms $\mathscr{L}_{evap}$ (·····); $\mathscr{L}_{wd} + \mathscr{L}_{diff}$ (• • •).

convective heat transfer ($\mathscr{L}_{conv}$) and the terms due to diffusion of water vapour ($\mathscr{L}_{wd} + \mathscr{L}_{diff}$). The figure shows that the two-way coupling term due to evaporation and the terms due to diffusion of water vapour are negligible and that the gas advection term is small compared to the remaining two terms. In the transient phase, the thermal diffusion term is not fully balanced by the sum of the gas convection term and the two-way coupling term, which results in an increasing gas temperature in the region close to the upper wall.

As can be expected from the shape of the temperature profile, the thermal diffusion term tends to raise the gas temperature. Since the particles can only be heated by heat transfer from the gas through two-way coupling, their temperature is lower than the gas temperature near the warm wall. Therefore, the two-way coupling term tends to lower the gas temperature. The gas convection term results in a small decrease of the gas temperature.

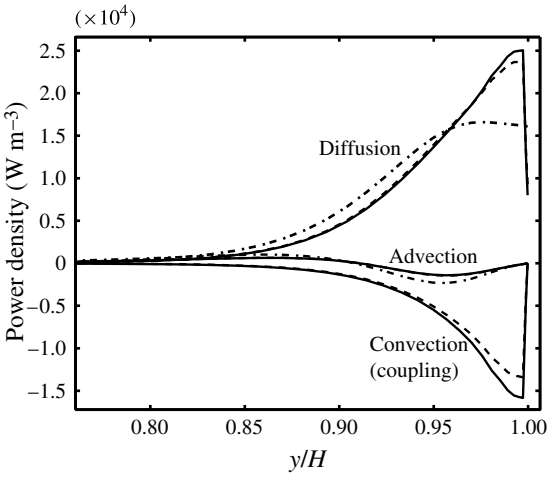

FIGURE 7. Terms in the energy equations as a function of the wall-normal coordinate close to the warm wall at $t^+ = 32$, showing diffusive fluxes (top), advection fluxes (middle) and convection coupling terms (bottom): reference case (——); case with solid particles (– – –); case without particles (–·–).

Now, we know which terms play a role in the change of the gas temperature in time. We compare the non-negligible terms, i.e. the gas convection and diffusive terms and the two-way coupling term due to convective heat transfer between the two phases, for the reference, solid and no particles cases in figure 7. This figure shows that the gas convection term is small for all three cases. The absence of the two-way coupling term in the case without particles explains why the temperature increase in this case is larger than in the other two cases. In the no particles case, the thermal diffusion term is smaller than in the reference and solid cases. However, since the two-way coupling term is absent in the no particles case, the sum of all terms in the gas temperature equation is larger than in the reference and solid cases and, hence, the increase of the gas temperature is larger. The difference in temperature between the reference case with water droplets and the case with solid particles is mainly caused by the two-way coupling term due to convective heat transfer. This term is larger in magnitude in the reference case than in the solid case because the evaporation in the reference case leads to a lower temperature of the dispersed phase. The resulting larger temperature difference between droplets and carrier gas increases the magnitude of the two-way coupling term.

The thermal properties of the air–water system depend on the initial temperature and, via the heat and mass transfer process, on the strength of the thermal forcing through the walls. This can be observed by comparing the high temperature case and high heat flux case with the reference case. The results of these two cases show some differences with respect to the reference case. In particular, the asymmetry in the mean gas temperature profile of the high heat flux case shown in figure 8 is due to the convex dependence of the saturation pressure on temperature expressed by Antoine's relation (2.20). The asymmetry of the temperature profile is not clearly visible in the reference and high temperature cases because of the small temperature difference between the two walls in the statistically steady state. Apparently, a higher overall temperature does not lead to strongly different normalized temperature profiles. When the temperature difference between the walls becomes larger, the asymmetry

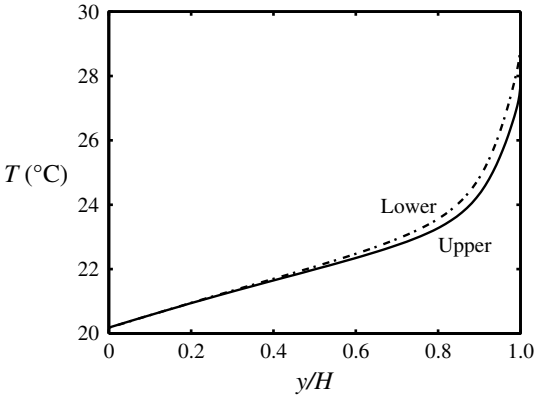

FIGURE 8. High heat flux case. Mean gas temperature as a function of the wall-normal coordinate in the statistically steady state: temperature in the upper half of the channel (——); mirror temperature in the bottom half of the channel (–·–).

of the temperature profile also becomes visible. This is reflected in the water vapour mass concentration as well. Apart from this, the results of the high heat flux case are very similar to those of the reference case. A larger difference in the heat transfer properties of the channel occurs in the high temperature case, i.e. for a higher initial temperature, and this will be analysed in the next section.

4.2. *Nusselt number*

In order to quantify the heat transfer properties in the statistically steady state, we introduce the Nusselt number, defined as

$$Nu = \frac{\left(\left. \dfrac{\mathrm{d}\langle T_g \rangle}{\mathrm{d}y} \right|_{wall} \right)}{\dfrac{\langle \Delta T_g \rangle}{2H}}, \tag{4.1}$$

where ΔT_g is the mean temperature difference between the walls. A larger Nusselt number implies that the fluid is able to transfer more heat between the walls given the same wall temperature difference. Such a process is better suited in a heat exchanger. In the transient regime, we define the Nusselt number as a function of time without averaging in time:

$$Nu(t) = \frac{\left(\left. \dfrac{\mathrm{d}\overline{T_g}}{\mathrm{d}y} \right|_{wall} \right)}{\dfrac{\Delta \overline{T}_g}{2H}}. \tag{4.2}$$

In figure 9, $Nu(t)$ is shown for the seven cases. As already explained in the previous subsection, we observe that the presence of particles or droplets leads to a larger value of the Nusselt number in the statistically steady state (compare reference, solid and no particles cases). Moreover, Nu depends on the initial channel temperature (compare reference and high temperature cases), but very little on the applied heat flux at the walls (compare reference and high heat flux cases). The droplet size and the volume fraction also have a direct effect on Nu, which will be analysed in detail.

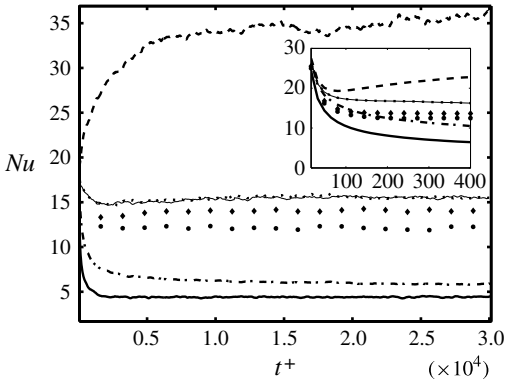

FIGURE 9. Nusselt number history for the seven cases: reference case (·····); high temperature case (– – –); high heat flux case (——); bigger droplets case (• • •); smaller volume fraction case (♦♦♦); solid particles case (–·–); no particles case (———). The inset zooms in on the initial behaviour.

Following Kuerten *et al.* (2011), we quantify the effect of particles and droplets on *Nu* by splitting it into various contributions. By averaging equation (2.7) over the homogeneous directions and over time in the statistically steady state and integrating the result twice over the wall-normal direction, we obtain the following expression for *Nu*:

$$Nu = 1 - \frac{1}{\alpha_g \langle \Delta T_g \rangle} \int_{-H}^{H} \langle u_y' T_g' \rangle \, \mathrm{d}y + \frac{1}{\langle \Delta T_g \rangle} \int_{-H}^{H} \int_{-H}^{y} \left\langle \frac{\mathscr{L}_{wd} + \mathscr{L}_{diff} + \mathscr{L}_{2way}}{k_g} \right\rangle \mathrm{d}s \, \mathrm{d}y. \quad (4.3)$$

Here $\alpha_g = k_g/(\rho_a c_{v,a} + \rho_v c_{v,v})$ is the thermal diffusivity, which is assumed constant in this paper. Moreover, $u_y' = u_y - \langle u_y \rangle$ is the fluctuating wall-normal component of the velocity of the gas, $T_g' = T_g - \langle T_g \rangle$ is the fluctuating gas temperature and $\langle \Delta T_g \rangle$ is the mean temperature difference between the two walls in the statistically steady state. In (4.3) the contributions from the water vapour diffusion terms $\mathscr{L}_{wd}$ and $\mathscr{L}_{diff}$ and from the two-way coupling term due to evaporation $\mathscr{L}_{evap}$ appear to be negligible, in agreement with the results shown in figure 6. For all cases considered, they contribute less than 0.1 % to *Nu*.

The contribution from $\mathscr{L}_{diff}$ can be analysed in more detail by writing it as

$$\begin{aligned}(R_a - R_v)\mathscr{D}(T_g - T_{\ell_0})\nabla^2 \rho_v \;=\; & (R_a - R_v)\mathscr{D}\nabla\rho_v \cdot \nabla(T_g - T_{\ell_0}) \\ & + (R_v - R_a)\mathscr{D}\nabla \cdot ((T_g - T_{\ell_0})\nabla\rho_v). \end{aligned} \quad (4.4)$$

The first term on the right-hand side is of the same form and magnitude as $\mathscr{L}_{wd}$. The second term can be integrated if the thermal conductivity is assumed constant to give a contribution to *Nu* equal to

$$Nu_{diff} = \frac{(R_v - R_a)\mathscr{D}}{k_g \langle \Delta T_g \rangle} \int_{-H}^{H} \left\langle (T_g - T_{\ell_0}) \frac{\partial \rho_v}{\partial y} \right\rangle \mathrm{d}y. \quad (4.5)$$

In order to analyse this term further, we write $(T_g - T_{\ell_0}) = T_0 + T_g'' - T_{\ell_0}$, where T_0 is the constant initial temperature. Since T_g'' is negative in the lower half of the channel and positive in the other half, while $\partial\rho_v/\partial y$ is positive throughout the channel, it

can be expected that the term with T_g'' in Nu_{diff} is very small. The numerical analysis of this term shows that it is three orders of magnitude smaller than Nu_{diff}. The contribution from $(T_0 - T_{\ell_0})$ can be integrated over y, which results in

$$Nu_{diff} \approx \frac{(R_v - R_a)\mathscr{D}(T_0 - T_{\ell_0})\langle \Delta\rho_v \rangle}{k_g \langle \Delta T_g \rangle}, \tag{4.6}$$

where $\langle \Delta\rho_v \rangle$ is the mean vapour mass density difference between the two walls in the statistically steady state. For the small temperature differences between the walls in our simulations, we can write

$$\langle \Delta\rho_g \rangle \approx \frac{\partial \rho_{v,sat}}{\partial T} \langle \Delta T_g \rangle, \tag{4.7}$$

since deviations from saturation are very small in the statistically steady state. The result is

$$Nu_{diff} \approx \frac{\partial \rho_{v,sat}}{\partial T} \frac{(R_v - R_a)\mathscr{D}(T_0 - T_{\ell_0})}{k_g}. \tag{4.8}$$

For the reference case and the high heat flux case, we find $Nu_{diff} \approx 0.003$, and for the high temperature case, the result is $Nu_{diff} \approx 0.03$, which shows that this contribution to the Nusselt number is indeed negligible.

Hence, the Nusselt number can accurately be expressed as $Nu = Nu_{lam} + Nu_{turb} + Nu_{part}$, where $Nu_{lam} = 1$ is the result for a laminar channel flow without particles,

$$Nu_{turb} = -\frac{1}{\alpha_g \langle \Delta T_g \rangle} \int_{-H}^{H} \langle u_y' T_g' \rangle \, \mathrm{d}y \tag{4.9}$$

is the contribution from turbulent transport and

$$Nu_{part} = \frac{1}{\langle \Delta T_g \rangle} \int_{-H}^{H} \int_{-H}^{y} \left\langle \frac{\mathscr{L}_{conv}}{k_g} \right\rangle \mathrm{d}s \, \mathrm{d}y \tag{4.10}$$

consists of the effect of the convective heat transfer between the two phases.

Table 2 shows that the presence of particles or droplets with a two-way coupling to the fluid flow does not significantly reduce the heat transfer due to turbulent transport. This differs from the results obtained by Kuerten *et al.* (2011) and can be explained by the different flow conditions, in particular the much smaller volume fraction of particles in the present simulations. Comparison of the reference, solid and no particles cases shows that the presence of particles leads to an increase of the Nusselt number of around 30 %. If droplets replace particles, the increase in Nusselt number is much larger: a factor of 3.5. For both droplets and particles, the increase is caused by the contribution from the convective heat transfer between the two phases, Nu_{part}. The simplified expression for Nu_{part} (Kuerten *et al.* 2011),

$$Nu_{part} \approx -\int_{-H}^{+H} \int_{-H}^{y} \frac{2\pi \langle n(s) d_i (T_g(\boldsymbol{x}_i, t) - T_i) \rangle}{\langle \Delta T_g \rangle} \, \mathrm{d}s \, \mathrm{d}y, \tag{4.11}$$

helps to understand this. The contribution from the convective heat transfer between the phases is large if the relative temperature is large in regions of the channel with a large concentration of the dispersed phase. Therefore, in the following, we

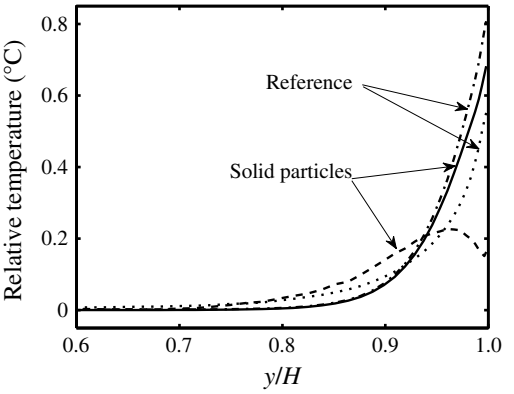

FIGURE 10. Relative temperature $\overline{(T_g(\boldsymbol{x}_i, t) - T_i)}$ as a function of the wall-normal coordinate near the warm wall: reference case at $t^+ = 400$ (·····); solid particles case at $t^+ = 400$ (– – –); reference case at $t^+ = 32$ (–·–); solid particles case at $t^+ = 32$ (——).

Case	Particles	Nu	Nu_{lam}	Nu_{turb}	Nu_{part}
Reference	Water droplets	15.6	1.0	3.0	11.6
High temperature	Water droplets	35.9	1.0	2.5	32.4
High heat flux	Water droplets	15.6	1.0	3.0	11.6
Bigger droplets	Water droplets	12.2	1.0	2.9	8.3
Smaller volume fraction	Water droplets	14.1	1.0	3.1	10.0
Solid	Solid particles	5.9	1.0	3.4	1.5
No particles	—	4.4	1.0	3.4	—

TABLE 2. Different contributions to the Nusselt number for all test cases.

analyse the temperature difference between the two phases and the concentration of particles/droplets.

Figure 10 shows the mean temperature difference $\overline{(T_g(\boldsymbol{x}_i, t) - T_i)}$ averaged over the homogeneous directions near the warm wall at two instances of time for the reference and solid cases. Note that $\overline{T_g(\boldsymbol{x}_i, t)}$ equals the mean temperature of the gas evaluated at the particle or droplet position. Since particles and droplets are preferentially located at locations where the gas temperature differs from its Eulerian mean, this temperature is not equal to the mean Eulerian gas temperature (Kuerten *et al.* 2011). The mean temperature difference near the warm wall is initially large for both the reference and solid cases. At $t^+ = 400$, the mean temperature difference is much smaller for solid particles than for droplets because evaporation cools the droplets.

In the statistically steady state, which starts later than the times shown in figure 10, the mean temperature difference is attenuated by the two-way coupling in both the reference and solid cases, resulting in the equilibrium mean relative temperature difference shown in figure 11. With solid particles, $\langle (T_g(\boldsymbol{x}_i, t) - T_i) \rangle / \Delta \overline{T}_g$ is larger than with droplets, apart from a small region very close to the walls. The relative temperature difference is multiplied by the particle concentration in expression (4.11) for Nu_{part}. Figure 12 shows that, in both cases, the majority of the particles are located very close to the walls. The integrand of (4.11) is shown in figure 13, where it appears that, in the vicinity of the wall, the product of particle concentration and

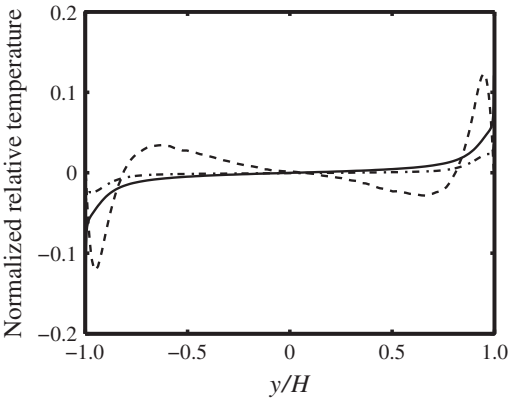

FIGURE 11. Plot of $\langle (T_g(\boldsymbol{x}_i, t) - T_i)\rangle / \langle \Delta T_g \rangle$ as a function of the wall-normal coordinate in the statistically steady state: reference case (–·–); high temperature case (——); solid particles case (– – –).

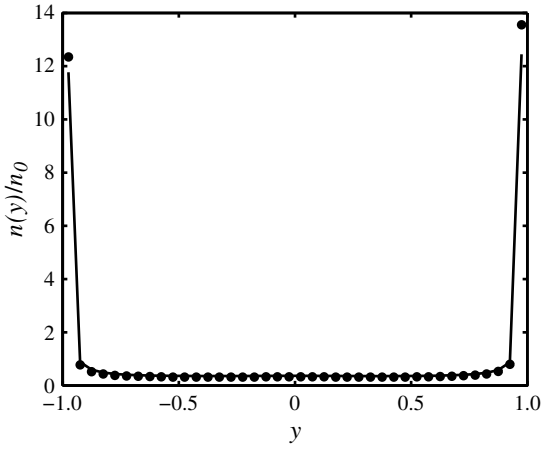

FIGURE 12. Droplet and particle concentration, $n(y)/n_0$, with n_0 the initial number of particles in a bin, as a function of the wall-normal coordinate in the statistically steady state: reference case (——); solid particles case (• • •).

relative temperature difference is much larger in the reference case than in the solid case. This is a direct consequence of the phase transition process of water droplets and it results in the observed eight times larger contribution to the Nusselt number from Nu_{part}.

The test cases with high temperature and high heat flux demonstrate the effect of variations in initial temperature and heat flux imposed at the walls on the heat transfer characteristics. The Nusselt number for the high heat flux case with the same initial temperature as the reference case but with a five times higher heat flux imposed at the walls is approximately the same as for the reference case. In contrast, the case with a high initial temperature results in a much higher Nusselt number. For the following reason, the rate of mass transfer near the walls is higher with a higher initial gas temperature. A given temperature change of a drop results in a bigger change in saturation vapour pressure at a higher gas temperature. The latter is easily seen

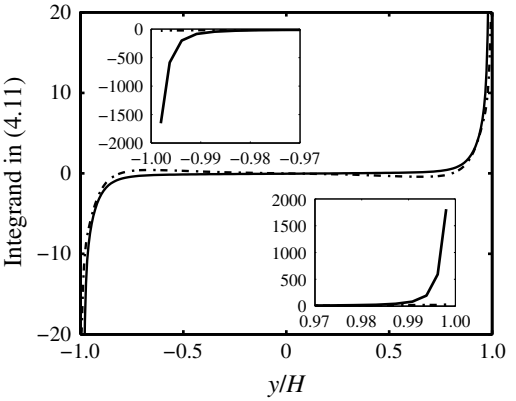

FIGURE 13. Integrand in expression (4.11) for Nu_{part} as a function of the wall-normal coordinate in the statistically steady state (averaged over $32\,000 < t^+ < 45\,000$) with a close-up view near the walls: reference case (——); solid particles case (–·–).

from the Clausius–Clapeyron equation or from the Antoine relation (2.20). Initially, in the simulations, the gas near the hot wall is heated by heat diffusion from the wall. The droplets increase in temperature by convective heat transfer from the gas and evaporation sets in. The higher the initial temperature, the higher is the rate of evaporation, for the above reasons. In the statistically steady state, the reference and high temperature cases have about the same droplet diameters near the walls but the gas temperature level is higher with a higher initial temperature and, hence, the mass transfer rate as well. The effective heat transfer rate between the two walls is increased by this process, and therefore the temperature difference between the two walls is less in the high temperature case than in the reference case, both cases having the same imposed heat flux at the walls. This lower temperature difference causes the higher Nusselt number found. The independence of the Nusselt number on the heat flux imposed at the walls shows that the temperature difference between the two walls in the statistically steady state is proportional to the imposed heat flux.

The two last test cases, one with bigger droplets and one with half the volume fraction of the standard case, serve to study the effect of variations in droplet size and volume fraction on the heat transfer characteristics. In figure 9, droplets with twice the diameter and the same volume fraction as the standard (reference) case are seen to lead to a smaller Nusselt number as compared to the reference case. To better understand this result, the two contributions, Nu_{part} and Nu_{turb}, given in table 2 are now analysed.

The simplified expression for Nu_{part} given by (4.11) consists of two quantities: (i) the temperature difference between droplets and gas; and (ii) the local droplet number density multiplied by the droplet diameter. These quantities, averaged in 40 bins in the wall-normal direction and over time during the steady state, are given in figures 14 and 15, respectively. The higher evaporation rate associated with the bigger droplets leads to a larger mean temperature difference between droplets and gas near the walls. However, since the volume fraction remains the same as compared to the reference case, quantity (ii) becomes approximately one-quarter of the reference case near the warm wall. This indicates that, for a given amount of water in the system, a value of the droplet diameter that maximizes the value of Nu_{part} can always be found. The smaller volume fraction case shows that, if the volume

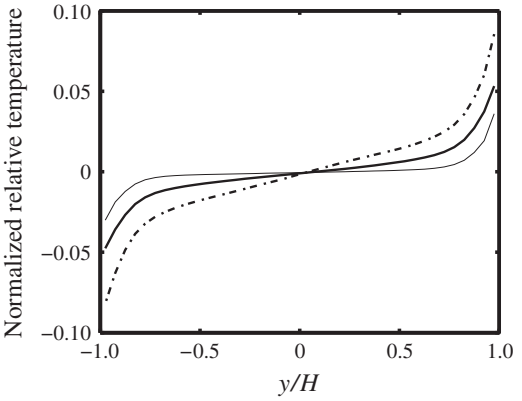

FIGURE 14. Plot of $\langle (T_g(\boldsymbol{x}_i, t) - T_i)\rangle / \langle \Delta T_g \rangle$ as a function of the wall-normal coordinate in the statistically steady state: reference case (——); bigger droplets case (–·–); smaller volume fraction case (——).

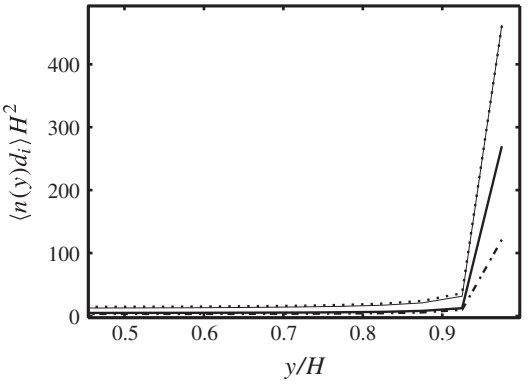

FIGURE 15. Plot of $\langle n(y) d_i \rangle H^2$ as a function of the wall-normal coordinate in the statistically steady state near the warm wall: reference case (——); bigger droplets case (–·–); smaller volume fraction case (——).

fraction is halved, then quantity (ii) becomes larger than half the corresponding one of the reference case. This is easily understood from the fact that at lower volume fractions turbophoresis is more manifest, while the mean temperature difference between droplets and gas increases, which compensates the decrease of Nu_{part} due to the smaller number of droplets in the channel. Therefore, for any given initial droplet diameter, a value of the volume fraction that maximizes the value of Nu_{part} can be found.

Here Nu_{turb} shows only a small change in both these cases. The largest change is observed for the high temperature case, which is, for this reason, taken in the following analysis of Nu_{turb}. Here Nu_{turb} depends on $\langle u_y' T_g' \rangle / \langle \Delta T_g \rangle$. However, velocity fluctuations of all test cases show only very small differences. This will be discussed in more detail later, in § 5. The main effect on Nu_{turb} arises from gas temperature fluctuations. Figure 16 shows $T_{rms}/\langle \Delta T \rangle$. At a higher temperature, evaporation rates are higher and, therefore, more water vapour is added to or taken from the gas, which attenuates gas temperature fluctuations. The higher evaporation rate of the

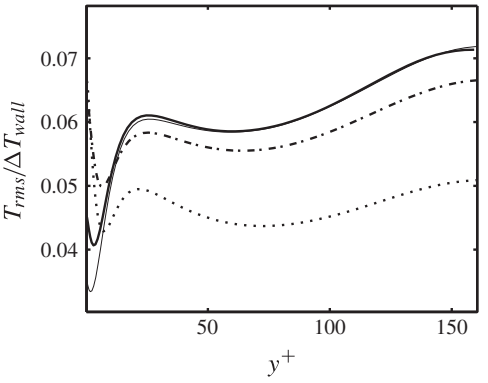

FIGURE 16. Plot of $T_{rms}/\langle\Delta T\rangle$ as a function of y^+ in the statistically steady state: reference case (——); bigger droplets case (–·–); smaller volume fraction case (——); high temperature case (·····).

bigger droplets decreases Nu_{turb} from 3.0 in the reference case to 2.9 in the bigger droplets case. Comparison of T_{rms} for the smaller volume fraction case with the reference case shows larger fluctuations with less droplets in the near-wall region but not elsewhere. This is easily understood from the fact that two-way coupling effects associated with mass transfer are less significant than in the reference case.

4.3. *Droplet size distribution*

In this subsection, we analyse the change in size of the droplets due to the thermal forcing applied to the channel. In figure 17, the mean droplet diameter history normalized by its initial value is plotted at three positions in the channel for the simulation of the reference test case. The three positions are the mid-plane of the channel and the first bins near the upper and lower walls. Obviously, near the heated wall the droplets start evaporating, resulting in a decreasing mean diameter, whereas the droplets near the cooled wall grow due to the condensation of water vapour. In the middle of the channel, the mean droplet diameter fluctuates around its initial value. For $t^+ > 0.5 \times 10^4$, the mean temperature difference between gas and droplets (figure 11) and, for $t^+ > 2.0 \times 10^4$, the droplet number density (figure 18) are constant in time and depend on the wall-normal coordinate. However, the root-mean-square (r.m.s.) of the droplet diameter in a certain bin, d_{rms}, increases at all times (see figure 19). If the same droplets were to remain in a bin, d_{rms} would not increase. This implies that there is a continuous inflow and outflow of droplets in a bin, as a consequence of turbulent transport.

Initially, the variance of the droplet diameter in the middle of the channel is smaller than near the walls (figure 19). This is caused by the fact that evaporation and condensation only occur close to the walls. The effect of droplet dispersion becomes evident in a later stage. The r.m.s. of droplet diameter did not yet saturate at $t^+ = 10 \times 10^4$. Simulating for an even longer period of time and including the explicit breakup of droplets that have grown beyond a certain size will clarify this. In the present work, the simulations have been kept sufficiently short to avoid the need to model the breakup of droplets.

At the final time of the simulation and close to the wall, the r.m.s. of the droplet diameter exceeds the change in mean droplet size over time. That implies that the

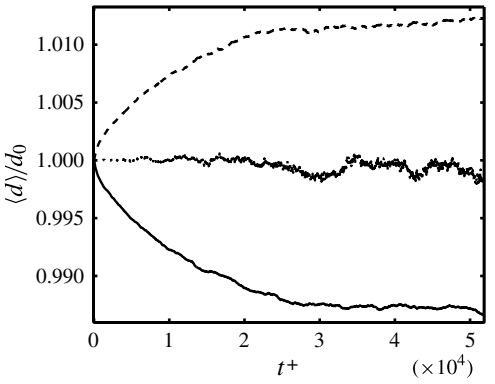

FIGURE 17. Reference case. Normalized mean droplet diameter history at three locations in the channel (d_0 = diameter at $t^+ = 0$): near the warm wall (——); mid-plane (·····); near the cold wall (– – –).

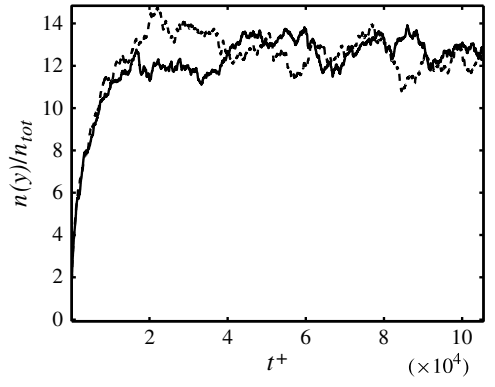

FIGURE 18. Reference case. History of droplet concentration, $n(y)/n_0$, with n_0 the initial number of particles in a bin, near the walls: near warm wall (——); near cold wall (– – –).

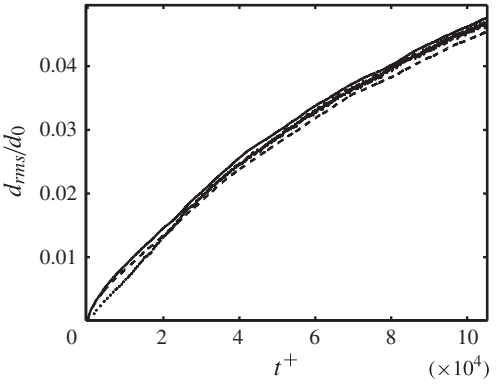

FIGURE 19. History of the droplet diameter r.m.s. at three locations in the channel: near the warm wall (——); mid-plane (·····); near the cold wall (– – –).

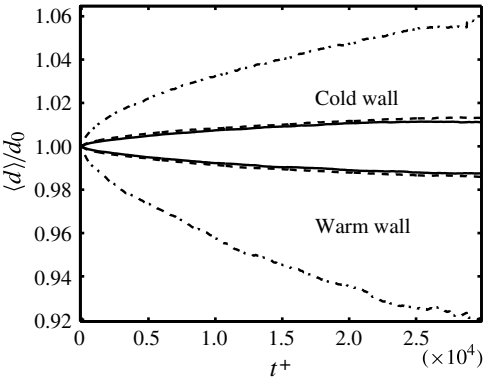

FIGURE 20. Normalized mean droplet diameter history near the cold and warm walls: reference case (——); high temperature case (– – –); high heat flux case (–·–).

probability density functions of droplet size of both walls overlap. This is a further illustration of the importance of turbulent transport of droplets through the channel.

Figure 20 shows the mean droplet diameter histories near the two walls for the reference, high temperature and high heat flux cases. The higher initial temperature does not affect the droplet mean diameter as much as the higher heat flux. On both walls, the reference and high temperature cases have an almost equal mean droplet diameter. In the high heat flux case, evaporation of the droplets near the warm wall and condensation of vapour on the droplets near the cold wall are enhanced by the higher temperature difference between the walls. In this case, the increase in mean droplet diameter near the cold wall is smaller than the decrease near the warm wall. The main reason for the asymmetry is the asymmetry of the gas temperature profile shown in figure 8. Figure 21 shows the r.m.s. of droplet diameter near both walls for the high temperature and high heat flux cases. With a higher heat flux, the r.m.s. near the cold wall is significantly smaller than near the warm wall but much larger than in the high temperature case. For a higher initial temperature, this difference is attenuated since the higher Nusselt number, due to the higher evaporation and condensation rates, leads to a smaller wall temperature difference.

Figure 17 shows that the mean droplet diameter has become approximately constant in time after $t^+ = 3.2 \times 10^4$. In this time, the mean flow has travelled approximately 250 times the length of the channel. The fact that the droplet concentration near the wall also is approximately constant for $t^+ > 20\,000$ (figure 18) indicates that equilibrium is established between condensation and evaporation, on the one hand, and water vapour heat flux across the channel, on the other. We investigate this in more detail in the next subsection.

4.4. *Droplet migration in the statistically steady state*

There are three mechanisms by which water can have a mean motion in the wall-normal direction of the channel: the first is molecular diffusion of water vapour by a mean concentration gradient, the second is turbulent transport of water vapour, and the third is mean motion of droplets in the wall-normal direction. In the statistically steady state, which is reached at $t^+ \approx 2.0 \times 10^4$, the mean droplet size and concentration do not change any more. Therefore, the three mechanisms should cancel each other out.

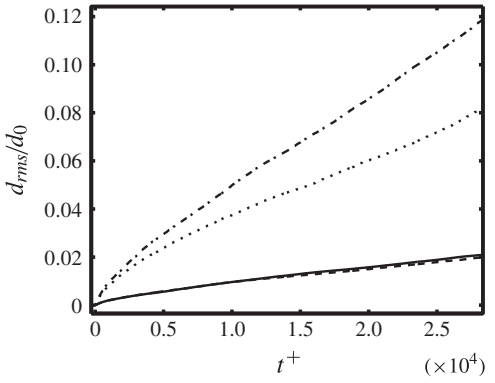

FIGURE 21. History of the droplet diameter r.m.s.: high temperature case near the warm wall (——); high temperature case near the cold wall (– – –); high heat flux case near the warm wall (–·–); high heat flux case near the cold wall (·····).

Since the water vapour concentration is higher at the warm wall than at the cold wall, there will be a net molecular diffusion flux of water vapour from the warm to the cold wall, which at all wall-normal positions in the channel is given by $-D\,\mathrm{d}\langle\rho_v\rangle/\mathrm{d}y$. The direction of the turbulent transport flux of water vapour, $\langle u_y'\rho_v'\rangle$, can be found in the following way. The water vapour concentration is correlated to the gas temperature (see figures 2 and 3) and, from the fact that Nu_{turb} is positive, we know that $\langle u_y'T_g'\rangle$ is negative. Therefore, the flux of water vapour by turbulent transport is also negative, i.e. directed from the warm to the cold wall. This implies that, for the three mechanisms to cancel each other out, there must be a net mass flux of water droplets from the cold to the warm wall, which balances the net mass flux of vapour from the warm to the cold wall. We write the total mass flux of water as $j_{water} = -D\,\mathrm{d}\langle\rho_v\rangle/\mathrm{d}y + \langle u_y'\rho_v'\rangle + j_{drops}$, where j_{drops} is the mass flux of water droplets, which can be directly calculated in the Lagrangian tracking of droplets adopted in our formulation.

Figure 22 shows the mass fluxes for the three mechanisms as functions of the wall-normal coordinate. The results are averaged over the two homogeneous directions and time in the statistically steady state. The calculation of j_{drops} is quite critical, for two reasons. First, although the droplet concentration near the walls has reached a statistically steady state at $t^+ \approx 20\,000$, the fluctuations in time are large. A very long time average is required to eliminate the effects of these fluctuations on j_{drops}. Second, the net mass flux of droplets is small. If only droplets with a positive wall-normal velocity component are considered, the mass flux is larger by two orders of magnitude. Hence, there is a very large 'traffic' of droplets to and from the walls separately, balancing almost perfectly and leaving a much smaller j_{drops} as a result. For these two reasons, the mass flux of the droplets is still quite irregular. Still, the results indeed underpin the picture described above. Both vapour mass fluxes are directed from the warm to the cold wall and are almost constant when added. The molecular diffusion is dominant in the near-wall regions, whereas the turbulent contribution takes over away from the walls. The net droplet mass flux is directed from the cold to the warm wall. This shows that there is a circulation of water. Water vapour moves from the warm to the cold wall, where it condenses onto droplets. The droplets move from the cold to the warm wall, where they evaporate again.

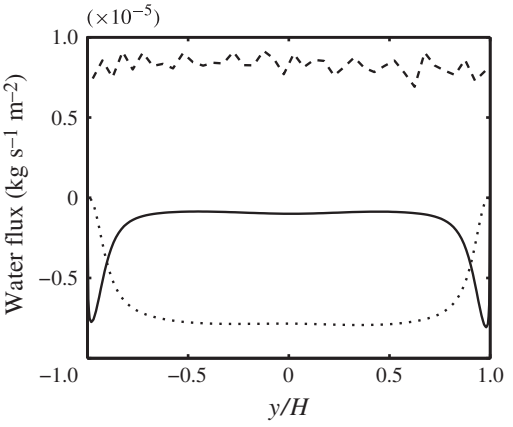

FIGURE 22. Water vapour and droplet mass fluxes as functions of the wall-normal coordinate in the statistically steady state (averaged over $21\,250 < t^+ < 85\,300$) in the reference case: water vapour mass flux due to Fick's law (——); water vapour mass flux due to turbulent diffusion $\langle v\rho_v \rangle$ (·····); droplet mass flux j_{drops} (– – –).

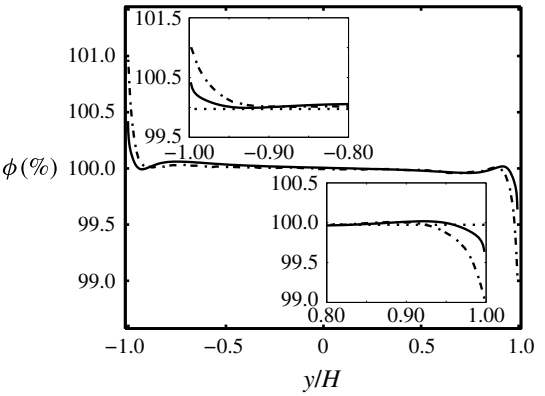

FIGURE 23. Reference case. Relative humidity (ϕ) history: steady state (averaged over $32\,000 < t^+ < 51\,000$) (——); $t^+ = 800$ (–·–).

The circulation model for water in the system is further supported by figure 23, which shows the relative humidity ϕ as a function of the wall-normal coordinate at various instances in time. The figure shows that ϕ is very close to 100 % in the majority of the channel. Only close to the walls can larger deviations from saturation be seen. In the transient stage, these deviations are smaller than 1 % and they are even smaller in the statistically steady state. Nevertheless, near the warm wall, ϕ is less than 100 %, so that net evaporation will occur; and close to the cold wall, the small supersaturation results in a net condensation of water vapour. If the mean droplet concentration observed in the steady state is constant, then the mean net flux of droplets measured by the number of droplets moving from one wall to the other one is zero. However, because droplets migrating from the cold wall to the warm wall are bigger in size than droplets migrating in the opposite direction, the mean net mass flux of water droplets cannot be zero and yields the calculated net mass flux.

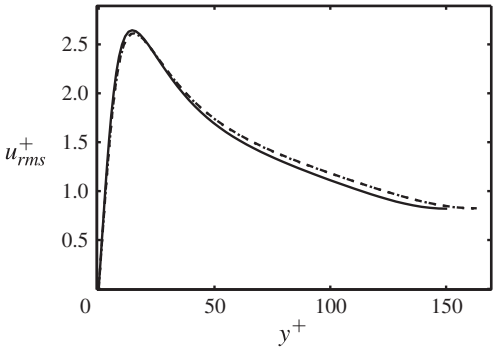

FIGURE 24. R.m.s. of the streamwise velocity component in the steady state: reference case with droplets (·····); with solid particles (– – –); without particles (——).

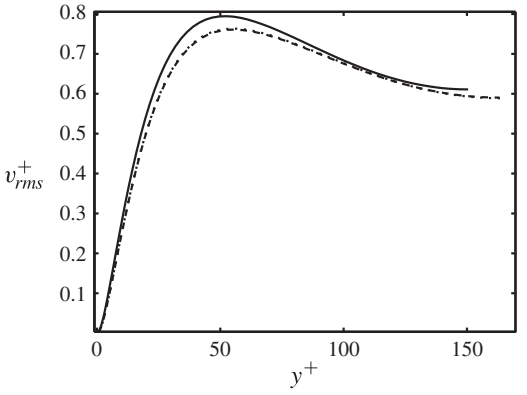

FIGURE 25. R.m.s. of the wall-normal velocity component in the steady state: reference case with droplets (·····); with solid particles (– – –); without particles (——).

5. Turbulence modulation

In this section, the effect of phase transition on the turbulence of the channel flow is analysed. We compare the modulation of turbulence caused by the presence of solid particles or evaporating droplets with the case without particles.

Turbulence modulation by particles is extensively reviewed by Eaton (2009) and Balachandar & Eaton (2010), with a remark on the limits of the point-particle method in predicting turbulence modulation when particles are comparable in scale to the small-scale turbulence. In our simulations, the particle size is smaller than the smallest Kolmogorov scale, also in the near-wall region. Figures 24–26 show the r.m.s. of the gas velocity components for the case without particles, the case with solid particles and the reference case with evaporating droplets. The presence of particles leads to a decrease of the turbulence kinetic energy. This result is in agreement with the results of Pan & Banerjee (1996) (in the absence of gravity), who reported attenuated turbulent intensities and Reynolds stresses for particles smaller than the dissipative length scale, whereas larger particles augment both intensities and stresses. In the following, the results of test cases with droplets are not shown since there are no significant differences between the turbulence modulation by solid particles and evaporating droplets. The same holds true for different initial temperature or boundary

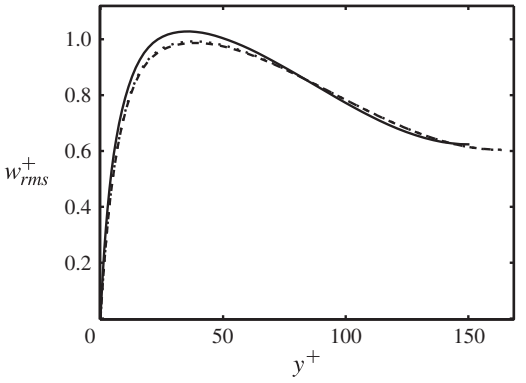

FIGURE 26. R.m.s. of the spanwise velocity component in the steady state: reference case with droplets (·····); with solid particles (– – –); without particles (——).

conditions, as in the high temperature case or high heat flux case. This negligible effect of phase transition is explained in the following analysis of the turbulence kinetic energy.

The turbulence kinetic energy is influenced by the presence of particles, especially in the vicinity of the wall where the particle concentration is higher in the steady state. Two-way coupling of momentum leads to an extra term in the turbulence kinetic energy (TKE) equation of the gas, associated with $\mathscr{L}_{\boldsymbol{u}}$ in (2.21). In the steady state, the production of turbulence kinetic energy in the gas is balanced by dissipation and particle dissipation due to the drag force between particles and gas, $\mathscr{L}_{\boldsymbol{u}}$:

$$-\int_{-1}^{+1} \underbrace{\langle u_j' u_k' \rangle \frac{\partial \langle u \rangle_j}{\partial x_k}}_{production} \,\mathrm{d}y = \int_{-1}^{+1} \underbrace{\left\langle \nu \frac{\partial u_j'}{\partial x_k} \frac{\partial u_j'}{\partial x_k} \right\rangle}_{dissipation\ \ \epsilon_k} \mathrm{d}y + \int_{-1}^{+1} \underbrace{\left(\left\langle \sum_{i=1}^{N} u_j \frac{\mathrm{d}(m_i v_{i,j})}{\mathrm{d}t} \delta(\boldsymbol{x} - \boldsymbol{x}_i) \right\rangle - \langle u_j \rangle \left\langle \sum_{i=1}^{N} \frac{\mathrm{d}(m_i v_{i,j})}{\mathrm{d}t} \delta(\boldsymbol{x} - \boldsymbol{x}_i) \right\rangle \right)}_{droplet\ \ dissipation} \mathrm{d}y. \tag{5.1}$$

Other terms in the TKE equation only transport kinetic energy within the channel and, therefore, their integrals over the wall-normal direction are equal to zero. Note that the quantity $\langle u_j \rangle$ in the droplet dissipation term is Eulerian averaged, whereas the other quantities are Lagrangian averaged. The quantity $\mathrm{d}(m_i v_{i,j})/\mathrm{d}t$ can be split into two contributions in the same way as (2.21). The contribution due to mass transfer arising from evaporation or condensation is negligible since the evaporation rate term is very small, as already shown in the gas temperature budget equation. Other studies, such as Mashayek (1998) and Wang & Rutland (2006), have shown that evaporation leads to an increase in the turbulence kinetic energy of the gas due to the transfer of kinetic energy from particles to gas and attenuation of particle dissipation because of the smaller mass loading ratio due to evaporation. These effects are important at high evaporation rates, which occur when starting a simulation from a non-equilibrium state. In our simulation the air–vapour gas is initially in equilibrium. Therefore, during

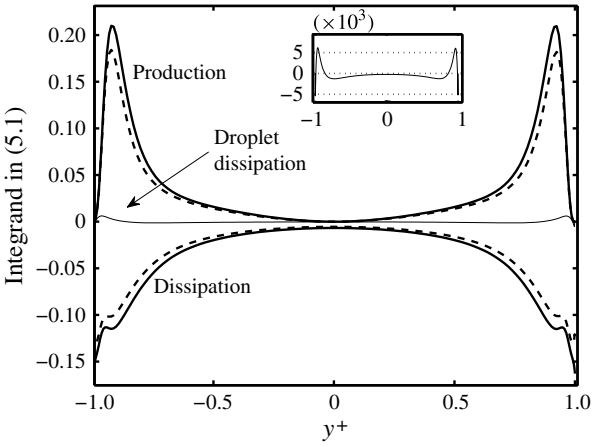

FIGURE 27. Integrands of terms in (5.1) in wall units versus y^+: case without particles (——); case with particle/droplets (– – –); droplet dissipation term (——).

the simulation of the transient phase, the boundary conditions applied result in small evaporation and condensation rates with a negligible effect.

In order to analyse the dissipative effect of the particles, the integrands of the terms in (5.1) are shown as functions of the channel height in figure 27 for the solid particles and without particles cases. The production and dissipation of turbulence kinetic energy decrease due to the presence of particles. Owing to the higher particle concentration, this is clearly visible near the walls. The droplet dissipation term in (5.1) is small compared to the other terms. The inset shows that this term produces turbulence kinetic energy near the walls and dissipates it in the core region of the channel. However, its integral is negative and, therefore, it has a dissipative effect globally.

The particle dissipation term is not the only cause for the particle dissipative effect on the gas. In the transient phase, this term is also small compared to the production and the dissipation terms. However, owing to the turbulence modulation of the particles, the turbulence kinetic energy production is almost immediately attenuated while the dissipation is still comparable to the case without particles. In addition, the droplet dissipation term adds extra dissipation, which yields a decrease in the turbulence kinetic energy that persists until the steady state is reached. The decrease of production is an indirect effect of the particle modulation of the gas velocity field. The mean gas streamwise velocity is accelerated by the presence of particles modulating $\partial\langle u\rangle/\partial y$ and, as already explained at the beginning of this section, also $\langle u'w'\rangle$ is modulated. Of these two contributions to the production term, the decrease of the Reynolds stress by the particles is the more important reason for the turbulence attenuation by the presence of particles.

6. Discussion and conclusions

In this paper, a numerical simulation method for water droplet-laden turbulent flow including heat and mass transfer by convection and phase change has been discussed. The model has been implemented in a pseudo-spectral DNS code for turbulent channel flow, where the droplets are modelled in a Lagrangian way. The effects of phase

change have been studied by comparison with results of a simulation in which only heat transfer between the phases is considered.

The results show that the boundary conditions applied to the initial state lead to evaporation and condensation. After a longer period of time, an equilibrium state is reached in which the relative humidity is close to 100 % over the total height of the channel. In the equilibrium state, the heat transfer between the two walls, quantified by the Nusselt number, is larger than in the case where the droplets are absent or replaced by solid particles with the same physical properties. Moreover, a further significant increase in Nusselt number has been found if the initial temperature of the channel is increased.

Apart from mean temperature, vapour mass density and relative humidity, the droplet size distribution has also been analysed. The mean droplet diameter is smaller near the warm wall than near the cold wall. When the mean diameter near the walls remains approximately constant in time, equilibrium between the vapour mass flux and droplet migration is established. The vapour flux from the warm wall to the cold wall is approximately balanced by droplet migration from the cold to the warm wall.

In the simulations that have been performed, nucleation of droplets and droplet breakup are ignored. Extension of the model with these mechanisms will be a topic of future research.

Acknowledgements

This research is supported by the Dutch Technology Foundation STW, Applied-Science Division of NWO (Netherlands Organization for Scientific Research), and the Technology Program of the Ministry of Economic Affairs of the Netherlands. Part of this work was sponsored by the Stichting Nationale Computerfaciliteiten (National Computing Facilities Foundation, NCF) for the use of supercomputer facilities, with financial support from the Nederlandse Organisatie voor Wetenschappelijk Onderzoek, NWO. We also acknowledge the support of COST Action MP 1106 on Smart and Green Interfaces.

REFERENCES

ANTOINE, C. 1888 Tension des vapeurs: nouvelle relation entre les tension et les temperatures. *Comptes Rendus* **107**, 681–684; 778–780; 836–837.

ARMENIO, V. & FIOROTTO, V. 2001 The importance of the forces acting on particles in turbulent flows. *Phys. Fluids* **13**, 2437–2440.

BALACHANDAR, S. & EATON, J. K. 2010 Turbulent dispersed multiphase flow. *Annu. Rev. Fluid Mech.* **42**, 111–133.

BEC, J., BIFERALE, L., LANOTTE, A. S., SCAGLIARINI, A. & TOSCHI, F. 2010 Turbulent pair dispersion of inertial particles. *J. Fluid Mech.* **645**, 497–528.

BIRD, R. B., STEWART, W. E. & LIGHTFOOT, E. N. 1960 *Transport Phenomena*. John Wiley & Sons.

CLIFT, R., GRACE, J. R. & WEBER, M. E. 1978 *Bubbles, Drops, and Particles*. Academic Press.

CROWE, C. T., SCHWARZKOPF, J. D., SOMMERFELD, M. & TSUJI, Y. 2011 *Multiphase Flow with Droplets and Particles*. CRC Press.

EATON, J. K. 2009 Two-way coupled turbulence simulations of gas–particle flows using point-particle tracking. *Intl J. Multiphase Flow* **35** (9), 792–800.

ELGHOBASHI, S. 1991 Particle-laden turbulent flows: direct simulation and closure models. *Appl. Sci. Res.* **48**, 301–314.

ELGHOBASHI, S. 1994 On predicting particle-laden turbulent flows. *Appl. Sci. Res.* **52**, 309–329.

ESMAEELI, A. & TRYGGVASON, G. 1998 Direct numerical simulations of bubbly flows. Part I. Low-Reynolds-number arrays. *J. Fluid Mech.* **377**, 313–345.

ESMAEELI, A. & TRYGGVASON, G. 1999 Direct numerical simulations of bubbly flows. Part II. Moderate-Reynolds-number arrays. *J. Fluid Mech.* **385**, 325–358.

FERRANTE, A. & ELGHOBASHI, S. 2003 On the physical mechanisms of two-way coupling in particle-laden isotropic turbulence. *Phys. Fluids* **15**, 315–329.

HINZE, J. O. 1956 Fundamentals of the hydrodynamic mechanism of splitting in dispersion processes. *AIChE J.* **1** (3), 289–295.

KUERTEN, J. G. M. 2006 Subgrid modeling in particle-laden channel flow. *Phys. Fluids* **18**, 025108.

KUERTEN, J. G. M., VAN DER GELD, C. W. M. & GEURTS, B. J. 2011 Turbulence modification and heat trasfer enhancement by inertial particles in turbulent channel flow. *Phys. Fluids* **23**, 123301.

LENERT, A., NAM, Y., YILBAS, B. S. & WANG, E. N. 2013 Focusing of phase change microparticles for local heat transfer enhancement in laminar flows. *Intl J. Heat Mass Transfer* **56** (1–2), 380–389.

MARCHIOLI, C., SOLDATI, A., KUERTEN, J. G. M., ARCEN, B., TANIÈRE, A., GOLDENSOPH, G., SQUIRES, K. D., CARGNELUTTI, M. F. & PORTELA, L. M. 2008 Statistics of particle dispersion in direct numerical simulations of wall-bounded turbulence: results of an international collaborative benchmark test. *Intl J. Multiphase Flow* **34** (9), 879–893.

MASHAYEK, F. 1997 Direct numerical simulations of evaporating droplet dispersion in forced low-Mach-number turbulence. *Intl J. Heat Mass Transfer* **41**, 2601–2617.

MASHAYEK, F. 1998 Droplet–turbulence interactions in low-Mach-number homogeneous shear two-phase flows. *J. Fluid Mech.* **367**, 163–203.

MASHAYEK, F. 2000 Numerical investigation of reacting droplets in homogeneous shear turbulence. *J. Fluid Mech.* **405**, 1–36.

MASHAYEK, F. & PANDYA, R. V. R. 2003 Analytical description of particle/droplet-laden turbulent flows. *Prog. Energy Combust. Sci.* **29**, 329–378.

MASI, E., SIMONIN, O. & BÉDAT, B. 2011 The mesoscopic Eulerian approach for evaporating droplets interacting with turbulent flows. *Flow Turbul. Combust.* **86** (3–4), 563–583.

MAXEY, M. R. & RILEY, J. J. 1983 Equation of motion for a small rigid sphere in a non-uniform flow. *Phys. Fluids* **26**, 883–889.

MILLER, R. S. 2001 Effects of non-reacting solid particle and liquid droplet loading on an exothermic reacting mixing layer. *Phys. Fluids* **13** (11), 3303–3320.

MILLER, R. S. & BELLAN, J. 1999 Direct numerical simulation of a confined three-dimensional gas mixing layer with one evaporating hydrocarbon-droplet-laden stream. *J. Fluid Mech.* **384**, 293–338.

MILLER, R. & BELLAN, J. 2000 Direct numerical simulation and subgrid analysis of a transitional droplet laden mixing layer. *Phys. Fluids* **12**, 650–671.

PAN, Y. & BANERJEE, S. 1996 Numerical simulation of particle interactions with wall turbulence. *Phys. Fluids* **8** (10), 2733–2755.

POPOV, Y. O. 2005 Evaporative deposition patterns: spatial dimensions of the deposit. *Phys. Rev.* E **71**, 036313.

REVEILLON, J. & VERVISCH, L. 2005 Analysis of weakly turbulent dilute-spray flames and spray combustion regimes. *J. Fluid Mech.* **537**, 317–347.

ROUSON, D. W. I. & EATON, J. K. 2001 On the preferential concentration of solid particles in turbulent channel flow. *J. Fluid Mech.* **428**, 149–169.

SIREGAR, D. P. & KUERTEN, J. G. M. 2013 Numerical simulation of the drying of inkjet-printed droplets. *J. Colloid Interface Sci.* **392**, 388–395.

TOSCHI, F. & BODENSCHATZ, E. 2009 Lagrangian properties of particles in turbulence. *Annu. Rev. Fluid Mech.* **41**, 375–404.

TRYGGVASON, G., SCARDOVELLI, R. & ZALESKI, S. 2011 *Direct Numerical Simulations of Gas–Liquid Multiphase Flows*. Cambridge University Press.

TURNS, S. R. 2006 *Thermal-Fluid Sciences: an Integrated Approach*. Cambridge University Press.

WANG, Y. & RUTLAND, C. J. 2005 Effects of temperature and equivalence ratio on the ignition of *n*-heptane fuel spray in turbulent flow. *Proc. Combust. Inst.* **30** (1), 893–900.

WANG, Y. & RUTLAND, C. J. 2006 Direct numerical simulation of turbulent flow with evaporating droplets at high temperature. *Heat Mass Transfer* **42**, 1103–1110.

VAN WISSEN, R. J. E., SCHREEL, K. R. A. M. & VAN DER GELD, C. W. M. 2005 PIV measurements of a steam-driven, confined, turbulent water jet. *J. Fluid Mech.* **530**, 353–368.